Using high frequency observations of δ^{13}C-CH_4 and δ^{2}H-CH_4 and uncertain regional isotopic signatures to estimate sources of UK methane emissions

Alice E. Ramsden[1,2], Anita L. Ganesan[2], Matthew Rigby[3], Chris Rennick[4], Tim Arnold[5,6], Emmal Safi[4], Edward Chung[4], Dafina Kikaj[4], Cameron Yeo[4,2], Dave Lowry[7], Pete Levy[8], Simon O'Doherty[3], Kieran M. Stanley[3], Dickon Young[3], Joe Pitt[3], Damien Martin[9], Morgan Lopez[10], Michel Ramonet[10], Grant L. Forster[11,12], Arnoud Frumau[13], and Alistair J. Manning[1]

[1]Met Office Hadley Centre, Exeter, UK
[2]School of Geographical Sciences, University of Bristol, Bristol, UK
[3]School of Chemistry, University of Bristol, Bristol, UK
[4]National Physical Laboratory, Teddington, UK
[5]Department of Earth and Environmental Sciences, Lund University, Lund, Sweden
[6]School of Geosciences, University of Edinburgh, Edinburgh, UK
[7]Department of Earth Sciences, Royal Holloway, University of London, Egham, UK
[8]Centre of Ecology and Hydrology, Penicuik, UK
[9]School of Physics, Ryan Institute's Centre for Climate and Air Pollution Studies, National University of Ireland Galway, Galway, Ireland
[10]Laboratoire des Sciences du Climat et de l'Environnement (LSCE-IPSL), CEA-CNRS-UVSQ, Université Paris-Saclay, 91191 Gif-sur-Yvette, France
[11]Centre for Ocean and Atmospheric Sciences, School of Environmental Sciences, University of East Anglia, Norwich, UK
[12]National Centre for Atmospheric Sciences, University of East Anglia, UK
[13]Netherlands Organisation for Applied Scientific Research (TNO), Petten, 1755 LE, Netherlands

Correspondence: Alice E. Ramsden (alice.ramsden@metoffice.gov.uk)

Abstract. Methane is emitted from a range of anthropogenic and natural sources, and identifying these sources is important for emissions monitoring and mitigation. Different sources emit methane with different isotopic signatures; however these signatures are often uncertain or vary spatially or temporally. Top-down inverse models can be used with measurement of methane mole fractions to estimate total emissions of methane from all sources. We present an inverse model for estimating regional fossil-fuel (FF) and non-fossil-fuel (non-FF) emissions concurrently, using isotope ratio observations and uncertain isotopic signatures. This method is highly adaptable and could be used to estimate emissions from any number of sources. Synthetic data tests with this method show that this model can accurately estimate FF and non-FF methane emissions across the UK, when isotopic source signatures are fixed at known values. However, emissions estimation becomes less accurate when source signature uncertainties rise above approximately 50% of their likely ranges. In a real-world test of this method, we estimated south-east UK FF and non-FF emissions using high-frequency δ^{13}C-CH_4 and δ^{2}H-CH_4 observations from one UK site, with source signature uncertainties reflecting our current understanding of these values. Results show a limited impact on emissions uncertainty or magnitude, when compared with output from an inversion using only mole fraction observations. This suggests that both the ongoing expansion of isotope ratio observations and an improved understanding of isotopic signatures is

required for this method to be used to estimate UK FF and non-FF methane emissions, with reduced uncertainty compared to traditional inverse methods.

1 Introduction

Global average atmospheric methane (CH_4) mole fractions have exceeded 1900 parts per billion (ppb, expressed as a dry air mole fraction) and are continuing to rise, with some of the largest annual increases on record occurring in the last 5 years (Lan et al., 2023). Improved mechanisms for monitoring these changes are required to find their causes and to evaluate current climate change mitigation measures. Inverse modelling of emissions using atmospheric observations, as demonstrated in this work, can contribute to this process.

Methane is a key target for emissions reduction because of its short tropospheric lifetime compared to other greenhouse gases (of approximately 10 years) yet relatively high 100-year global warming potential of 28 times that of carbon dioxide (Myhre et al., 2013). A rapid reduction in emissions of methane into the atmosphere could have a substantial impact on overall climate forcing (Ganesan et al., 2019), and is likely required to meet global climate change targets, including those set out in the Paris Agreement. The Agreement aims to keep the mean global temperature rise to below 2°C above pre-industrial temperatures, and in doing so, is requiring all signatories to regularly report on emissions targets. To aid with setting these emissions targets, the Intergovernmental Panel on Climate Change (IPCC) has produced Shared Socio-economic Pathways (SSPs) which detail various emission scenarios and their impact on future global temperature rises (Arias et al., 2021). However, recent global atmospheric methane concentrations do not reflect the decline required to meet the lower-emission SSPs. Therefore, greater focus on the monitoring of country-level methane emissions is required to monitor progress towards these targets (Nisbet et al., 2019).

Accurate quantification of country-level methane emissions is complicated by its wide range of anthropogenic and natural sources. For the period 2010-2019, global average methane emissions were estimated to be approximately 560 teragrams per year (Tg y^{-1}) using top-down methods. Approximately 40% of these global emissions are believed to originate from natural sources: wetlands, freshwater lakes and rivers, permafrost, and geological seeps (Saunois et al., 2025). As most of the methane from these natural sources is emitted during the decomposition of organic matter by methantrophic organisms in waterlogged environments, these sources are highly seasonal and can be dependent on soil temperature and moisture (Pison et al., 2013). The remaining 60% of emissions are expected to be from anthropogenic sources, with agriculture and waste management (including enteric fermentation by livestock, manure management, landfills and waste water treatment) comprising approximately 40% of total emissions. Fossil fuel production, transportation and use contribute to approximately 20% of total emissions (Saunois et al., 2025). Biomass and biofuel burning also contribute relatively low emissions of methane.

Methods used to estimate global, regional and country-level methane emissions can be broadly split into two main types (Leip et al., 2018; Saunois et al., 2025): bottom-up studies, which model emissions processes to directly estimate sector-level surface emissions using biogeochemical models or geographic and economic data; and top-down inverse modelling studies, which improve on an initial (prior) estimate of emissions by using an atmospheric transport model to infer total surface

emissions from atmospheric methane mole fraction (concentration) observations. Sector attribution in top-down estimation is challenging and often cannot be carried out using only information from methane mole fraction observations (Ganesan et al., 2019), although some studies have attempted to attribute net fluxes to particular sectors based on bottom-up estimates of the flux spatial distribution e.g. Tunnicliffe et al. (2020); Lunt et al. (2021).

Bottom-up methods are regularly used by national governments to compile national inventories. These inventories can then be reported to, for example, the United Nations Framework Convention on Climate Change. Top-down models have more commonly been used by the scientific community to learn about trends in global emissions (e.g. Maasakkers et al. (2019); Zhang et al. (2021)), study regional emissions and their sources (e.g. Ganesan et al. (2015); Sheng et al. (2018)) or measure emission rates from large point sources (e.g. Cui et al. (2019)). More recently, top-down models have been used as independent verification of bottom-up national GHG inventories (Henne et al., 2016; Manning et al., 2021) and newer international research projects often include direct collaboration between top-down modelling scientists and national inventory teams (e.g. PARIS (2023) and AVENGERS (2023)).

1.1 Using methane isotope ratio observations for source attribution

Recent developments in top-down inverse modelling methods, including those presented in this paper, have allowed for a more detailed comparison of top-down and inventory estimates of emissions, by estimating sector-level emissions directly during the inversion. These methods often use observations of secondary trace gases (e.g. C_2H_6 or CO) or methane isotope ratio (e.g. δ^{13}C-CH_4 or δ^{2}H-CH_4) to aid with source attribution. Methane is created by a range of production mechanisms, some of which produce distinct ratios of co-emitted gases or isotopologues. The source of emissions can be inferred when these characteristic ratios are detected in observations. For example, ethane is co-emitted from methane's fossil fuel sources, but there is negligible emission from methane's biogenic sources, so observations of ethane can be used to infer a fossil fuel methane source in local methane plume studies, e.g. Mielke-Maday et al. (2019) or regional inverse modelling, e.g. Barkley et al. (2021). See Ramsden et al. (2022) for a more detailed summary of the use of secondary mole fraction observations in methane inverse modelling; the rest of this paper will focus on the use of methane isotope ratio observations for source attribution in top-down modelling of methane emissions.

Methane from biogenic (agriculture, waste and wetland) sources contains a lower ratio of ^{13}C to ^{12}C than methane from thermogenic (fossil fuel) sources, so observations of the ^{13}C:^{12}C ratio can be used to infer the proportion of sources contributing to total emissions. Similarly, ^{2}H:H observations can be used for source attribution because biological methane sources are more depleted in heavier hydrogen isotopologues than fossil fuel methane sources. These characteristic ratios are known as source signatures. Observations of these isotope ratios are provided as delta values (δ^{13}C-CH_4 and δ^{2}H-CH_4) which are referred to below and are explained in more detail in Section 2.2.

Due to the availability of long term, low frequency (weekly or monthly) isotope ratios observations, these observations have most commonly been used in the top-down modelling of methane emissions on a global scale, to attribute trends in emissions to a source sector (e.g. Schaefer et al. (2016); Lan et al. (2021); Riddell-Young et al. (2025b)). Methane isotope ratio observations have also been analysed using the Keeling plot and Miller-Tans techniques to find the δ^{13}C-CH_4 isotopic

source signature of plumes measured during aircraft transects (France et al., 2016; Cain et al., 2017) and of regional methane sources (Menoud et al., 2021; Varga et al., 2021; Hoheisel and Schmidt, 2024). Menoud et al. (2021) found that the use of δ^2H-CH_4 observations, alongside δ^{13}C-CH_4, provided useful additional source information for their case study in Krakow, Poland where there was overlap between locally observed fossil fuel and microbial source signatures in δ^{13}C-CH_4 but not in δ^2H-CH_4. Similarly, Röckmann et al. (2016) demonstrated how new high-resolution δ^{13}C-CH_4 and δ^2H-CH_4 observations at Cabauw in the Netherlands could be used to improve source attribution of western European emissions, and found results that contradicted a bottom-up model's source allocation. When using δ^{13}C-CH_4 observations, Zazzeri et al. (2017) and Saboya et al. (2021) also found top-down estimates of methane emissions from London (in the UK) which contradicted those from a bottom-up UK inventory; source attribution using the isotope ratio observations led to the conclusion that under-reported local gas leaks were responsible for the mismatch.

Isotopic source signatures can vary spatially and temporally depending on the type of production processes or composition of reaction products leading to methane emission (Sherwood et al., 2017). More recent databases of source signatures have improved current understanding of source signatures, including Riddell-Young et al. (2025a) and Milkov et al. (2020) for fossil fuel sources, Menoud et al. (2022) for European sources, Bakkaloglu et al. (2021) for UK landfill sources and Lowry et al. (2020) for a range of UK sources.

Recent advances in top-down modelling using isotope ratio observations include consideration of the uncertainty in our knowledge of source signatures. Thanwerdas et al. (2022, 2024) presented a global inverse modelling method using a modified version of the Community Inversion Framework (CIF) with weekly or monthly smoothed observations of methane, δ^{13}C-CH_4 and δ^2H-CH_4 to optimise both global methane emissions and their associated source signatures. Drinkwater et al. (2023), using inverse methods to optimise both regional emissions and regional δ^{13}C-CH_4 signatures, concluded that a relative increase in tropical methane was causing the recent trend in global methane. They also found strong trends and variation in regional signatures across all regions of the globe between 2004 and 2020. Basu et al. (2022) incorporated both methane mole fraction and δ^{13}C-CH_4 observations into a global inversion model using the transport model TM5-4DVAR, but instead of optimising source signatures directly in the inversion as in Thanwerdas et al. (2022), they explored the impact of source signature uncertainty by running the inverse model with different configurations of fixed source signatures. Overall, previous works using isotope ratio observations have shown potential for use in providing more independent top-down attribution of emissions to their source, but have also highlighted that the use of single isotope ratio tracers may limit a model's ability to separate sources when there is overlap between source signatures or when source signatures are uncertain. This uncertainty has been considered in some cases, but often is not factored into the final emissions estimates and their uncertainties.

This paper aims to build on these previous works by presenting a novel inverse modelling method that uses new high-frequency observations of both δ^{13}C-CH_4 and δ^2H-CH_4 and incorporates uncertainty in regional signatures in estimates of methane emissions from fossil fuel (FF) and biogenic, non fossil fuel (non-FF) sources. This model is adapted from work presented in Ramsden et al. (2022) which used observations of methane and ethane mole fractions and optimised both methane emissions and ethane:methane emission ratios. The modifications made to this method to incorporate isotope ratio observations and regional signatures are presented in Section 2 alongside a more general introduction to the inverse modelling framework.

The potential of this method to estimate UK fluxes using methane and methane isotope observations from the UK observational network is tested in a range of synthetic data tests. This is followed by a short case study using the new dataset of UK high frequency methane isotope observations, to demonstrate how this model could be used to estimate regional FF and non-FF methane emissions. Conclusions from these experiments and future developments with this model, including the use of the model with a wider network of new methane isotope observations developed as part of the Horizon Europe PARIS (Process Attribution of Regional Emissions) project, are discussed in the final sections of this paper.

2 Methods

This section briefly introduces top-down inverse modelling of surface emissions for different sectors, before discussing how this framework is adapted to include methane isotope ratio observations and source signatures.

2.1 Modelling emissions from multiple sectors

An atmospheric transport model is used to link atmospheric mole fraction observations to surface emissions. As observed mole fractions represent the sum of global background mole fractions and enhancements from local sources, both of these quantities need to be considered when estimating regional emissions. This system can be represented by the forward model:

$$\mathbf{y} = \mathbf{H} \cdot \mathbf{x} + \mathbf{H}_{bc} \cdot \mathbf{x}_{bc} + \boldsymbol{\epsilon}_y \tag{1}$$

where $\mathbf{y}$ is a vector of atmospheric observations made at times t and $\mathbf{H}$ is the combined prior emissions and atmospheric transport sensitivity matrix. $\mathbf{H}$ has dimensions of [t, N] where the study domain has been split into a set of N grid cells at a coarser resolution than the transport model (this is discussed in more detail in Section 2.3.3). A scaling factor ($\mathbf{x}$) is estimated for each of these N grid cells over each inversion period. $\mathbf{H}_{bc}$ is the combined boundary conditions and atmospheric transport from the boundaries to each observation location, with dimensions of [t, M boundaries]. A scaling factor $\mathbf{x}_{bc}$ is estimated for each of the M boundaries. ϵ_y is the combined model and measurement error.

This model can be expanded to include emission estimates for multiple sectors (s), all of which contribute to the total observed mole fraction:

$$\mathbf{y} = \begin{bmatrix} \mathbf{H}_1 & \dots & \mathbf{H}_s & \mathbf{H}_{bc} \end{bmatrix} \cdot \begin{bmatrix} \mathbf{x}_1 \\ \vdots \\ \mathbf{x}_s \\ \mathbf{x}_{bc} \end{bmatrix} + \boldsymbol{\epsilon}_y \tag{2}$$

where each $\mathbf{H}_1$ ... $\mathbf{H}_s$ has dimensions of [t, N], and each $\mathbf{x}_1$ ...$\mathbf{x}_s$ has dimensions of [N].

2.2 Modelling emissions from multiple sectors using isotope ratio observations

Methane isotope ratio measurements are presented in delta notation, which is a ratio of the major containing isotope to the minor containing isotope (in the methane sample), relative to an international standard. Isotope ratios used in this work are expressed as δ^{13}C-CH_4 and δ^{2}H-CH_4, and typically reported as per mille deviations):

$$\delta_i = \left(\frac{R_i}{R_{std,i}} - 1 \right) \tag{3}$$

where i is the isotope ratio of interest and $R_{std,i}$ is the isotopic standard. For δ^{13}C-CH_4, $R_{std,13}$ is the Vienna PeeDee Belemnite (VPDB) standard with a value of 0.011180 and for δ^{2}H-CH_4, $R_{std,2}$ is the Vienna Standard Mean Ocean Water (VSMOW) standard with a value of 0.00015575 (Werner and Brand, 2001; Brand et al., 2010).

Isotope ratio observations are influenced by the mixture of regional sources and background values. Unlike in Equations 1 and 2, a non-linear forward model is required to represent the relationship between emissions, source signatures and observed isotope ratios:

$$\mathbf{y}_i = \mathbf{F}_s \left(\mathbf{x}_s, \boldsymbol{\delta}_{s,i} \right) + \mathbf{F}_{bc} \left(\mathbf{x}_{bc}, \boldsymbol{\delta}_{bc,i} \right) + \epsilon_i \tag{4}$$

where $\mathbf{y}_i$ is a vector of the modelled isotope ratios, $\mathbf{F}_s$ is a function that combines transport matrices and prior emissions, scaling factors and source signatures for each sector (s), $\mathbf{x}_s$ contains the emissions scaling factors for each sector and $\delta_{s,i}$ contains the source signatures for each sector. $\mathbf{F}_{bc}$ is a function that combines transport matrices, prior boundary conditions, boundary condition scaling factors and boundary condition isotope ratios. $\mathbf{x}_{bc}$ contains the boundary condition scaling factors and $\boldsymbol{\delta}_{bc,i}$ contains the boundary condition 'signatures', which link mole fractions and isotope ratios at the boundaries. This model applies to both isotope ratio observations used in this study.

Methane emission estimates are linked to observed isotope ratios using isotopic source signatures in a multi-step process. First, modelled mole fractions of total methane are created from the transport matrices, emissions and boundary condition priors. Then information from the source signatures and boundary 'signatures' is used to scale the total modelled mole fractions into modelled mole fractions of each isotopologue. The ratio of these isotopologue mole fractions is converted into a modelled isotope ratio, which can be compared to the observed isotope ratios. Whilst the isotope ratios measured at the boundaries do not have 'source signatures' in the same sense as the emissions which have distinct sources, in this work we use representative 'signatures' for the boundaries, which provide the relationship between methane mole fractions and isotope ratios at each boundary of the domain.

In practice, the modelled isotope ratios are created using this process:

1. The fraction (**a**) of each isotopologue as a proportion of the total methane mole fraction is calculated from the vectors of source signature isotope ratios using the following equations (derivations of these equations are given in detail in

Appendix A):

$$\mathbf{a}_{^{12}\mathrm{CH_4},s} = \frac{1}{(1+\mathbf{R}_{13,s}+\mathbf{R}_{2,s})}$$
$$\mathbf{a}_{^{13}\mathrm{CH_4},s} = \frac{1}{\left(1+\frac{1}{\mathbf{R}_{13,s}}+\frac{\mathbf{R}_{2,s}}{\mathbf{R}_{13,s}}\right)}$$
$$\mathbf{a}_{^{12}\mathrm{CH_3D},s} = \frac{1}{\left(1+\frac{1}{\mathbf{R}_{2,s}}+\frac{\mathbf{R}_{13,s}}{\mathbf{R}_{2,s}}\right)} \quad (5)$$

where $\mathbf{R}_{13,s}$ and $\mathbf{R}_{2,s}$ are the isotope ratios for each sector *s*, derived from δ^{13}C-CH_4 and δ^{2}H-CH_4 source signatures, using Equation 3 rearranged. The source signatures, and therefore isotope ratios, are all vectors at the same spatial and temporal resolution as the emissions scaling factors (with dimensions of [*N*]).

2. The fraction of each isotopologue at each boundary of the inversion domain ($\mathbf{a}_{bc,j}$) are produced using Equations 5 with vectors of boundary 'signatures' ($\mathbf{R}_{13,bc}$ and $\mathbf{R}_{2,bc}$), which have dimensions of [*M*].

3. The modelled mole fractions for each isotopologue (*j*) are created using:

$$\mathbf{y}_j = \begin{bmatrix}\mathbf{H}_1 \cdot \mathbf{m} & \dots & \mathbf{H}_s \cdot \mathbf{m} & \mathbf{H}_{bc,j}\end{bmatrix} \cdot \begin{bmatrix}\mathbf{a}_{1,j}\mathbf{x}_1 \\ \vdots \\ \mathbf{a}_{s,j}\mathbf{x}_s \\ \mathbf{a}_{bc,j}\mathbf{x}_{bc}\end{bmatrix} \quad (6)$$

where *s* is the number of emission sectors, **x** contains the emission scaling factor terms and **m** is a mass conversion term. Each $\mathbf{H}_s$ contains the combined transport and emissions term, with dimensions of [*t*,*N*], as discussed above. Each $\mathbf{H}_s$ contains emissions which are converted from mass units typically found in inventories (g m^{-2} s^{-1}) to molar units (mol m^{-2} s^{-1}), using an average methane molar mass of 16.043 g. As this method suggests different contributions of methane istopologues to the total emission, this molar mass will change and the molecular weight for this conversion depends on the different proportions of isotopologues as follows:

$$\mathbf{m} = \mathbf{a}_{^{12}\mathrm{CH_4}} M_{r,^{12}\mathrm{CH_4}} + \mathbf{a}_{^{13}\mathrm{CH_4}} M_{r,^{13}\mathrm{CH_4}} + \mathbf{a}_{^{12}\mathrm{CH_3D}} M_{r,^{12}\mathrm{CH_3D}} \quad (7)$$

4. The isotope ratios are calculated from the ratio of these isotopologue mole fractions:

$$\mathbf{R}_{^{13}CH_4} = \frac{\mathbf{y}_{^{13}CH_4}}{\mathbf{y}_{^{12}CH_4}} \quad (8)$$

$$\mathbf{R}_{^{12}CH_3D} = \frac{\mathbf{y}_{^{12}CH_3D}}{\mathbf{y}_{^{12}CH_4}} \quad (9)$$

5. These ratios are converted into modelled isotope ratios using the delta value equation (Equation 3).

A Bayesian statistical framework is used to find a posterior distribution of emissions and boundary conditions from this non-linear system. As in previous studies (Ganesan et al. (2014); Ramsden et al. (2022)) a hierarchical form of Bayes' theorem is used, which allows for secondary parameters, such as emission ratios of a gas and a tracer, model uncertainty and regional isotope ratio signatures (from here on referred to as regional signatures) to also be optimised during the inverse modelling process:

$$\rho(\mathbf{x}_s, \mathbf{R}_{s,i}, \boldsymbol{\sigma}, \boldsymbol{\sigma}_i | \mathbf{y}, \mathbf{y}_i) \propto \rho(\mathbf{y}, \mathbf{y}_i | \mathbf{x}_s, \mathbf{R}_{s,i}, \boldsymbol{\sigma}, \boldsymbol{\sigma}_i) \cdot \rho(\mathbf{x}_s) \cdot \rho(\mathbf{R}_{s,i}) \cdot \rho(\boldsymbol{\sigma}, \boldsymbol{\sigma}_i). \tag{10}$$

where observations of methane ($\mathbf{y}$) and methane isotope ratio ($\mathbf{y}_i$) and model uncertainty for methane ($\boldsymbol{\sigma}$) and methane isotope ratio ($\boldsymbol{\sigma}_i$) are all included. See Section 2.3.1 and Ganesan et al. (2014) and Ramsden et al. (2022) for more information on the model error hyper-parameter.

The hierarchical model allows for non-Gaussian probability density functions (PDFs) to be specified for all input parameters. For example, truncated Gaussian PDFs can be used for those parameters for which negative values are unrealistic or uniform PDFs can used for parameters which are not well constrained.

Markov chain Monte Carlo (MCMC) with a Metropolis-Hastings algorithm is used to form the posterior distributions (Ganesan et al., 2014; Ramsden et al., 2022). The first 50% of samples are discarded as a 'burn-in' period, to reduce any impact of the model's initial state on the posterior, and every 100^{th} value of the remaining trace is retained to form a posterior distribution. Convergence is tested at multiple steps by comparing the percentage and absolute differences between the mean of the previous 40% and 20% of iterations. The percentage difference between the first and second halves of the posterior traces are also compared to confirm convergence. The mean and 15.9^{th} and 84.1^{st} percentiles (one standard deviation) of the posterior traces are used as the presented statistics for ~~for~~ the emissions, regional signatures and boundary condition scaling factors.

2.3 Model inputs

This method was tested first using synthetic data, before being used with a new set of methane δ^{13}C-CH_4 and δ^{2}H-CH_4 observations from the Heathfield (HFD) tall tower site approximately 65 km south-east of London in the UK (Rennick et al., 2021; Safi et al., 2024; Rennick et al., 2025) to estimate monthly emissions in the south-east UK across 2022 and 2023. This section gives more detail on these observations and the other model inputs that were used during both the synthetic data tests and UK case study.

2.3.1 Observations

High frequency methane observations were used from four sites in the UK Deriving Emissions Linked to Climate Change (DECC) network: tall tower sites at Tacolneston (TAC), Ridge Hill (RGL), Heathfield (HFD) and Mace Head (MHD) on the west coast of Ireland (Stanley et al., 2018; Stavert et al., 2019). Observations from two Integrated Carbon Observation System (ICOS) sites were also used: Weybourne (WAO) in South-East England and Cabauw (CBW) in the Netherlands. Mole fraction measurements at MHD, TAC, RGL, HFD and CBW were made using Picarro cavity ring-down spectroscopy (CRDS)

instruments, while measurements at WAO combined Picarro data with measurements from an in situ Fourier Transform Infrared Spectrometer. All measurements were calibrated on the same scale. Figure 1 shows the locations of these sites.

Methane δ^{13}C-CH_4 and δ^2H-CH_4 isotope ratio observations were taken at the HFD site using the 'Boreas' preconcentration system coupled to a dual-laser spectrometer (Rennick et al., 2021). Unlike previous methane isotope ratio instruments, which often required weekly flask samples to be transported to a lab for isotopic analysis, this preconcentration system allows for the spectrometer to directly measure mole fractions of $^{12}CH_4$, $^{13}CH_4$ and $^{12}CH_3D$ in-situ at high frequency (approximately one hour intervals). These mole fractions were then converted to an isotope ratio. More detail on this instrumentation is available in Rennick et al. (2021) and Safi et al. (2024).

Throughout this work, all observations were averaged into 4-hourly means. This time scale was chosen as a compromise between computation time, suitable variability in emissions and in the model's ability to represent transport and mixing at this resolution.

For the UK case study, observations were also filtered before use in the inversion. The four-hourly averaged methane observations were filtered to remove times when the transport model was assumed to perform less accurately, or when local emissions were contributing strongly to the observed mole fractions. Data points were removed if over 15% of the area-integrated sensitivity at the site was from the 25 $0.23^\circ \times 0.35^\circ$ grid cells surrounding the site (at the native resolution of the transport footprints). Observations were also removed if the planetary boundary layer height (as estimated by the Numerical Weather Predication model use to drive the transport model) was within 100 m of the observation height at the observation time. Filtering varied from month to month, but on average these filters removed between 29% and 38% of observations from TAC, RGL, HFD and WAO. On average, fewer observations were removed from the MHD, and CBW sites (23% and 14%, respectively). Methane isotope ratio observations were then filtered to remove any timestamps without concurrent methane mole fractions observations, as these are required to produce the modelled isotope ratios. On average, 38% of δ^{13}C-CH_4 and δ^2H-CH_4 observations were removed before use in each monthly inversion. As an example, Fig. C1 shows the number of observations available before and after filtering for each inversion month at HFD.

The standard deviation of the observations within the four-hour averaging period was used as a combined measure of measurement and representativeness uncertainty (henceforth referred to as measurement uncertainty). When only one observation was available during an averaging period, the median uncertainty across the whole month was instead used as the uncertainty for that averaging period. Across the case study months and all sites with available observations, mean measurement uncertainty was 8.15 ppb for methane. δ^{13}C-CH_4 and δ^2H-CH_4 uncertainty from HFD was on average 0.25 ‰ and 1.82 ‰.

Model uncertainty was included as the maximum of either an optimised scaling factor of the pollution event size at each timestamp, or a pre-defined minimum error (see Table 1 for these values). A model uncertainty scaling factor was optimised for each gas/isotope ratio at each site, for each monthly inversion period. These model uncertainty scaling factors were given uniform prior PDFs, with limits as stated in Table 1. The pollution event size at each timestamp, for CH_4, δ^{13}C-CH_4 and δ^2H-CH_4 at each site, was calculated as the difference between the measured value and the modelled baseline, at the current MCMC iteration. Posterior mean model uncertainty was, on average across the case study period and across all sites with available observations, approximately 30% of the methane pollution event size. Posterior mean methane isotope ratio model uncertainty

	Minimum uncertainty	PDF limits (min, max) (% of pollution event)
CH_4	40 ppb	(0, 1.0)
δ^{13}C-CH_4	0.05 ‰	(0, 0.5)
δ^{2}H-CH_4	0.05 ‰	(0, 0.5)

Table 1. Parameters used for the model error minimum and model error uniform PDFs.

was approximately 22% for δ^{13}C-CH_4 and 24% for δ^{2}H-CH_4. Combined model-measurement uncertainty for each observation was calculated by taking the root mean square of the current sample of the model uncertainty and the measurement uncertainty. The squares of these values (the variances) were then used to fill the diagonal of the model-measurement uncertainty matrix for each species.

2.3.2 Transport footprints

Transport footprints, representing the relationship between surface emissions and atmospheric mole fractions, were generated using the Met Office's Numerical Atmospheric-dispersion Modelling Environment (NAME) (Jones et al., 2007), a Lagrangian particle dispersion model. With methane's approximately 10-year atmospheric lifetime, it is assumed that loss of methane via chemical reaction is negligible over the monthly modelling periods. NAME used meteorological fields to simulate the movement of 20,000 inert gas particles from each measurement location back in time for 30 days, recording their interactions with the surface and their exit location from the model domain. NAME was driven by UK-specific 1.5 km horizontal resolution one-hourly temporal resolution meteorological fields over the UK and Ireland and by Unified Model three-hourly resolution fields over the rest of the study domain (Walters et al., 2014). Hourly transport footprints were produced at a spatial resolution of $0.23^\circ \times 0.35^\circ$over the domain of 10.7°N to 79.3°N, 97.9°W to 39.7°E. These footprints were then averaged at the same four-hour temporal resolution as the observations. As discussed in Section 2.3.4 below, information from the transport footprints on where and when modelled particles exit the study domain were used to create modelled background concentrations.

2.3.3 A priori emissions and inversion grid setup

An initial (a priori) estimate of annual mean UK emissions from the fossil-fuel (FF) and non-fossil-fuel (non-FF) sectors was taken from the Centre for Ecology and Hydrology (CEH) UK Greenhouse Gas (UKGHG) model of disaggregated UK methane emissions, which is based on nationally reported flux totals (Levy, 2020). For a priori fluxes outside the UK, annual mean flux estimates were taken from the Emissions Database for Global Atmospheric Research (EDGAR) v8.0 (European Commission, Joint Research Centre (JRC), the International Energy Agency (IEA), 2023). Figure 2 shows an example year (2023) of these a priori fluxes and lists the UKGHG and EDGAR sectors that contribute to the aggregated FF and non-FF sectors. In this work, we have not included prior estimates of natural methane fluxes (e.g. from wetlands or freshwater), because in the UK all land is categorised as 'managed' and emissions from all areas are included in the national inventory.

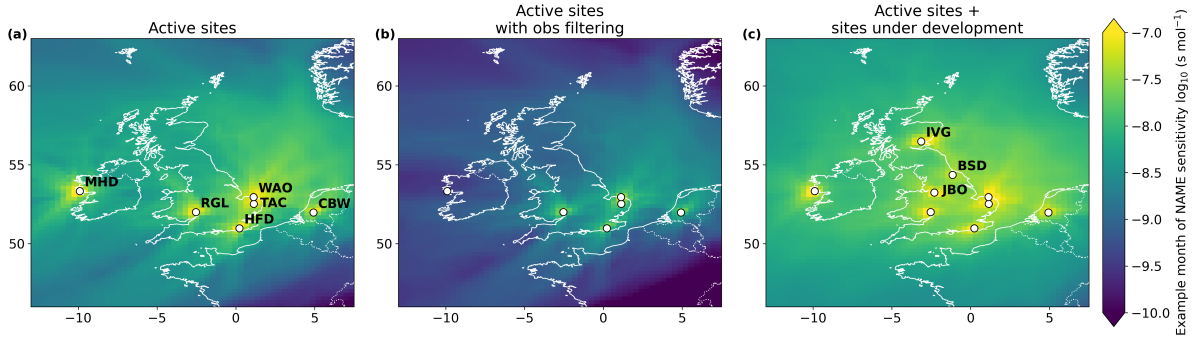

Figure 1. An example month of NAME sensitivity footprints: for May 2023 with all observations from the current network of sites used in this work (a); for May 2023 with observations from the current network, filtered based on meteorological conditions, as used in the UK case study (b); and for May 2024 from the recently expanded network of sites as included in the synthetic study (c).

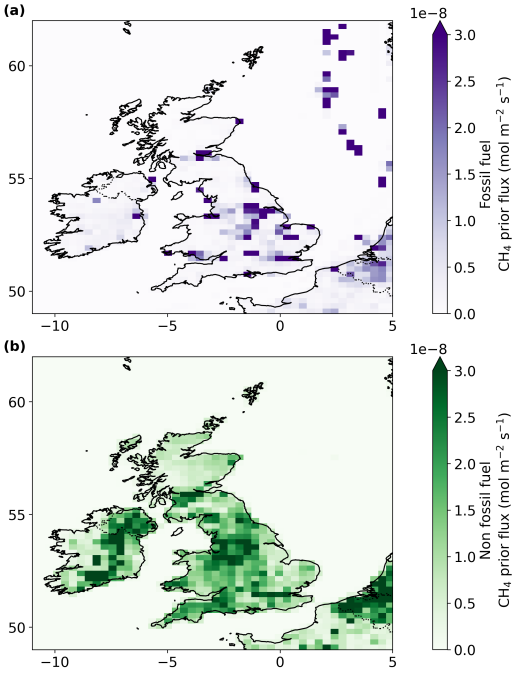

Figure 2. A priori 2023 CH_4 fluxes from CEH's UKGHG model and EDGAR, for the FF **(a)** and non-FF **(b)** sectors. The FF prior includes fluxes from domestic and industrial combustion and processes, energy production and use and transport. The non-FF prior includes fluxes from enteric fermentation, manure management, waste water treatments, landfills and waste burning.

In both the synthetic data tests and UK case study, scaling factors of the a priori fluxes were optimised on a lower spatial resolution than the transport footprints or a priori fluxes. For the synthetic data test, a simple uniform grid of 81 cells was applied

over the UK, so emissions were only estimated over this area. For the UK case study, the whole inversion domain was split into approximately 100 spatial basis functions, and a scaling factor was optimised for each cell. These cells were chosen using a quadtree algorithm, which placed a higher density of smaller cells in areas where there is greater sensitivity to emissions and in areas where emissions are higher (see Western et al. (2021) for more detail on this process). This spatial distribution of cells was kept constant throughout the process by using the average sensitivity across all 24 inversion months to inform the quadtree algorithm, enabling a clear comparison of spatial emissions month to month. Before this quadtree algorithm was applied, the outermost areas of the inversion domain, where sensitivity to fluxes is low, was divided into 6 regions. An emissions scaling factor was optimised for each of these larger regions, alongside the approximately 100 smaller regions closer to the study area. Figure 3 gives the two inversion grid setups for the synthetic data test and UK case study.

Emission scaling factors were given truncated Gaussian prior PDFs, with means of one and standard deviations of one, equivalent to a 100% uncertainty on the a priori emissions in each inversion grid cell, truncated at zero to prevent negative emissions.

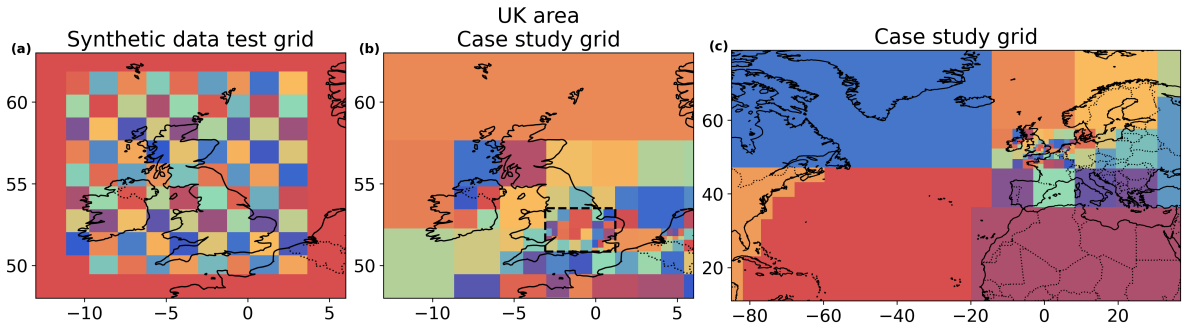

Figure 3. Spatial distributions of optimised regions, used in the synthetic data tests (a) and case study (b,c). The centre (b) and right (c) plots are identical, with the centre plot a zoomed in section over the UK, showing how the quadtree algorithm places more regions in areas of greater sensitivity to emissions. The dashed black line shows the area over which emissions are estimated, during the case study - the south UK area (SUK). Colours used in this plot have no meaning and are just used to differentiate between adjacent basis regions.

2.3.4 A priori boundary conditions

A boundary condition scaling factor was optimised for each of the transport model's domain boundaries, for each 7 day period within an inversion month. These higher frequency scaling factors, relative to the monthly emissions, were chosen to account for the seasonal cycles in background methane concentrations. An a priori estimate of mole fractions entering the study domain was created for each North, South, East and West curtain of the study domain. For methane, these a priori boundary conditions were based on the 25^{th} percentile of mole fraction observations each month from the Mace Head (MHD) site, which is situated on the west coast of Ireland and commonly samples background air from across the North Atlantic. When combined with information from the atmospheric transport model, these boundary conditions provided an apriori modelled 'background'

	FF emissions (‰)	non-FF emissions (‰)	Boundary condition (‰)
δ^{13}C-CH_4	-40 (-45, -35) 3	-60 (-75, -45) 5	-48 (-49, -46) 0.5
δ^{2}H-CH_4	-160 (-180, -125) 10	-280 (-350, -240) 20	-90 (-105, -85) 4

Table 2. Parameters used for the regional signature and emission ratio truncated Gaussian prior PDFs, given as: mean (min, max) standard deviation.

mole fraction for each observation point used in the study. Boundary condition scaling factors were given Gaussian prior PDFs, with standard deviations leading to equivalent uncertainties in the methane boundary conditions of 2%.

2.3.5 A priori regional source signatures and boundary isotope ratios

For the UK case study, regional isotopic signatures for δ^{13}C-CH_4 and δ^{2}H-CH_4 for each sector were optimised at two spatial scales: either with only one value per sector, for every month; or at the same spatial and temporal scale as emissions scaling factors: a FF and a non-FF value for each of the 6 outer regions and for each of the approximately basis function cells across the study domain, per inversion month. A third test was carried out with regional isotopic signatures fixed at their a priori means, which are identical across all regions, for each sector.

The means, standard deviations and ranges of the truncated Gaussian regional signature prior PDFs used are given in Table 2. These PDF parameters where chosen based on the Royal Holloway database of UK source signatures (Lowry et al., 2020; Menoud et al., 2022) which contains 286 measurements of δ^{13}C-CH_4 from a range of sources across the UK: landfill and waste management centres, agricultural ruminants and their waste, gas leaks, mines and roads. These data were combined with a further database of source signatures, compiled during the isoMET project (Dasgupta et al., 2025a, b). Figure A1 presents these data for each source category, as histograms and spatially mapped average signatures, at the resolution of the transport model. Whilst this database does contain information about spatial variation in these signatures, the observed signatures were collected from point sources which may not represent the average signature across a wider area, as optimised by the inversion. Therefore, in this work we used a spatially uniform a priori regional signature, with each regional isotopic signature using the same prior PDF per sector. Data on δ^{2}H-CH_4 source signatures was available from the isoMET database, but is more limited, as shown in Fig. B1.

Boundary condition δ^{13}C-CH_4 'signatures', which represent the average isotopic signature of methane entering the study domain, were given Gaussian prior PDFs, with a mean of -48 ‰ and a standard deviation of 0.5 ‰. These values were based on δ^{13}C-CH_4 flask observations at MHD (Michel et al., 2023) which were gathered as part of the National Oceanic and Atmospheric Administration (NOAA) Global Monitoring Laboratory (GML) Carbon Cycle Cooperative Global Air Sampling Network, and analysed at the Institute of Arctic and Alpine Research (INSTAAR) Stable Isotope Laboratory. Boundary condition δ^{2}H-CH_4 signatures were given Gaussian prior PDFs, with a mean of -90 ‰ and a standard deviation of 4 ‰. Independent flask observations of δ^{2}H-CH_4 are not currently taken at MHD, so the average 95^{th} percentile of Boreas observations at HFD was used to inform the δ^{2}H-CH_4 boundary condition prior.

2.4 Synthetic data experiments method

A range of synthetic data tests were carried out to explore the inverse model's ability to successfully attribute UK methane emissions to their source categories, using observations from the UK's GHG monitoring network. These tests used observations from six long-established active sites (MHD, TAC, RGL, HFD, WAO and CBW) as discussed above, and three new or reinstated UK sites: the newly-established Scottish Observatory for Atmospheric Research at the Balruddery Research Farm near Invergowrie (IVG) in Scotland (https://blogs.ed.ac.uk/soar/); the Jodrell Bank Observatory (JBO) tower, in Cheshire, north-west England; and the Bilsdale (BSD) tall tower site in north-eastern England, which is currently being recommissioned after a fire at the observation tower closed the site in 2021. The IVG site has a Picarro CRDS instrument to measure methane and an Aerodyne dual laser spectrometer for δ^{13}C-CH_4 measurement. It will have a Medusa GC-MS to measure ethane (amongst many other trace gases) and a Boreas system for δ^{13}C-CH_4 and δ^{2}H-CH_4 measurements. The JBO site has a Picarro CRDS instrument to measure methane, and the BSD site will have a Picarro CRDS instrument when it is reinstated. JBO and IVG have been running for a short time, so do not have the long period of observations required for the UK case study, but have been included here to demonstrate the potential of the UK network in the near future. Figure 1 shows the locations of the three newly updated sites, with an example month of modelled atmospheric transport footprints.

For these tests, synthetic mole fraction observations were created for each site by combining a priori FF and non-FF flux estimates from the CEH UKGHG methane database (see section 2.3.3) with atmospheric transport footprints (see section 2.3.2). For simplicity, only UK emissions were modelled in these synthetic data tests; boundary conditions and emissions from other areas in the model domain were not used to create the synthetic observations and no background mole fractions were included. To simulate measurement and model error, noise was added to these synthetic observations, proportional to the size of the mole fractions at each site. This prevented the added noise from over-impacting low mole fraction sites (such as MHD and CBW). Added noise was created by scaling the synthetic observations at each site by a randomly sampled value from a Gaussian distribution with a mean of zero and a standard deviation of 0.1. This equated to random noise of between 0 and 10% of the synthetic methane observations. Synthetic δ^{13}C-CH_4 and δ^{2}H-CH_4 observations were created using steps outlined in section 2.2, with spatially uniform regional signatures of -40 ‰ and -58 ‰ for FF and non-FF sources. These values were chosen based on the Royal Holloway University of London database of UK isotope source signatures as discussed above. Random noise was added to the synthetic isotope ratio observations, using a sampled Gaussian distribution with a standard deviation of 0.05 ‰ . Combined model-measurement error was set at the same size as the noise added to each set of synthetic observations. No filtering was applied to the observations, to produce a 'best case' scenario, where there was the maximum information available from the observations.

To test whether the inverse model could successfully use these observations to attribute methane fluxes to their two sources, the model was given incorrect a priori flux estimates, created by perturbing the flux fields used to produce the synthetic observations. A successful version of the model would be able to produce emissions scaling factors that transformed this perturbed flux prior into the 'true' fluxes as contained in the synthetic observations. For each of the 81 inversion grid cells shown in Fig. 3 (a), the 'true' emissions within each cell were scaled by a different value, randomly sampled from a uniform

distribution between 0.5 and 1.5. This simulates a scenario where a priori fluxes are up to 50% incorrect, relative to the fluxes used to produce the observations. The model then solved for 81 emissions scaling factors at the same spatial scale as the perturbation field, for each of the FF and non-FF sectors.

Emissions scaling factors were given Gaussian prior PDFs with a standard deviation of 1.0 (equivalent to 100% uncertainty on the a priori fluxes), truncated at zero to prevent the model from converging on negative scaling factors.

The model was initially run with only methane observations, where the model can only rely on the spatial distribution within the a priori emissions to infer information about sources. Then the inverse model was run with different combinations of methane isotope ratio observations and prior regional signatures. Four different setups were used: fixed, correct regional signatures; a variable regional signature per sector, with their priors perturbed from the true values by +25% for the FF sector and -75% for the non-FF sector; a variable regional signature per inversion grid cell, with the priors randomly perturbed from the true values to produce prior signatures within the central 50% of the PDFs used in the UK case study; and a variable regional signature per inversion grid cell, with the priors randomly perturbed from the true values to produce prior signatures within the full limits of the PDFs used in the UK case study. The randomly perturbed regional signature priors for the last two tests were created in a similar way to the perturbed emissions priors: a uniform distribution was sampled for each inversion grid cell, and the ‘true‘ regional signature in that cell was scaled by the sampled value to create the perturbed prior. These uniform distributions were selected to produce prior signatures either within the central 50% of the range or the whole range of the prior PDFs used in the UK case study (as shown in Table 2). All tests with perturbed regional signatures simulate a range of scenarios with realistic levels of regional signature uncertainty, considering our current understanding of UK source signatures.

The first test with synthetic methane isotope ratio observations was run with only δ^{13}C-CH_4 then with both δ^{13}C-CH_4 and δ^{2}H-CH_4, to illustrate the importance of including both type of isotope ratio observations.

Each test was repeated for three months, March-May 2024, to capture a range of possible sensitivities caused by differing wind directions across the UK. The differences between the posterior and ’true‘ emissions fields from the three repeats of each test were combined to find the average root mean square error (RMSE) between posterior and true FF and non-FF methane fluxes, across the UK.

3 Results

3.1 Synthetic data experiments

Figure 4 shows the combined posterior emissions estimates from all repeat runs of each inverse model setup with synthetic data (left to right), for the FF sector (top row), non-FF sectors (bottom row). Locations of the observation sites used are given as circles, coloured based on the type of observations available at each site. Grid cells of lighter colour, where RMSE is closer to zero, show areas where the model was more able to correctly replicate the ‘true’ flux field.

The methane-only model (Fig. 4 (a, g)) was unable to replicate the true emissions for either sector for the majority of the UK. There is some accurate estimation of non-FF emissions in central and eastern England and in central Scotland, where

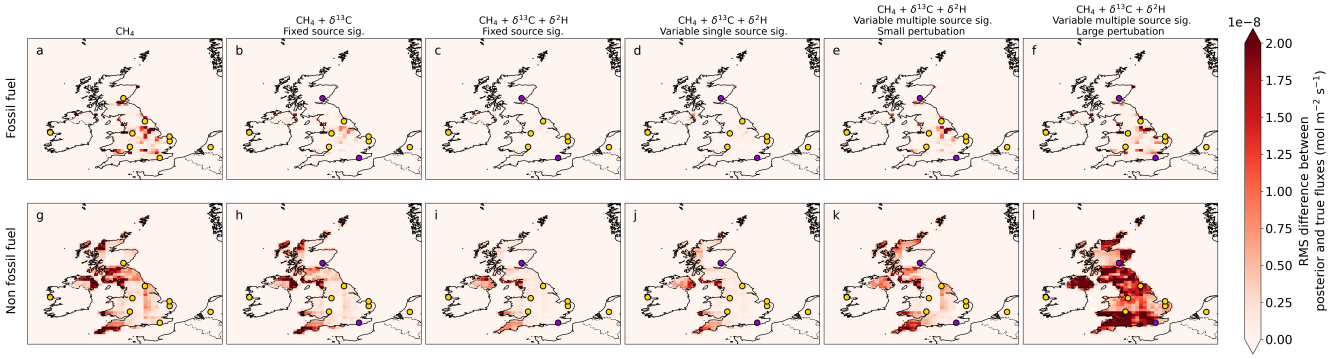

Figure 4. RMSE between the posterior and 'true' emissions, from synthetic data tests carried out with expanded UK observation network, for the FF (top) and non-FF (bottom) sectors, from the inverse model with: only CH_4 (a,g); CH_4 and δ^{13}C-CH_4 with fixed, correct regional signatures (b,h); CH_4, δ^{13}C-CH_4 and δ^2H-CH_4 with fixed, correct regional signatures (c, i); one variable signature per sector (d, j); one variable signature per grid cell, where the signature priors are randomly perturbed within the central 50% of the prior PDF range used for the UK case study (e, k); one variable signature per grid cell, where the signature priors are randomly perturbed within the whole range of the prior PDF range used for the UK case study signatures (f, l). Coloured dots show observation locations for: only CH_4 (yellow) and CH_4 and CH_4 isotope ratios (purple).

sensitivity to emissions is good. But in other areas the model did not adjust emissions from the prior mean and emissions estimates are inaccurate.

Most models with methane isotope ratio synthetic observations yield an improved estimate of the true emissions fields, for most of the UK, compared to results from the methane-only model. However, the spatial extent of this success, and the ability to accurately estimate emissions from both sectors depends on the observations used and the regional signature uncertainty.

Fixing regional signatures, at the 'true' values used to produce the synthetic observations, produced the most accurate estimates of FF and non-FF emissions. The test with this setup and only δ^{13}C-CH_4 observations (b, h) led to some inaccurate estimation of emissions in western areas of the UK, where sensitivity to emissions is lower. Including synthetic observations of both δ^{13}C-CH_4 and δ^2H-CH_4 in this test resolves this issue and emissions are estimated correctly for both sectors, apart from the most western coasts of the UK where there are still some inaccuracies in non-FF emissions estimates (c, i). From this result, and previous studies showing the importance of including both δ^{13}C-CH_4 and δ^2H-CH_4 observations when available (as discussed above), further synthetic tests were only carried out with both δ^{13}C-CH_4 and δ^2H-CH_4 synthetic observations.

The tests with a perturbed regional signature prior per sector simulate a scenario in which we assume a single signature per sector with some uncertainty but without any spatial variation (i.e. a single signature applies to the whole of the UK for each sector). The synthetic data test with this setup (d, j) was as successful as that with fixed regional signatures (c, i) and the model was able to adjust the perturbed regional signatures back to their 'true' values, reproducing both the 'true' emissions fields and modelled ~~isotope ratio~~ isotope ratios which matched the 'true' synthetic observations.

The tests with perturbed regional signature priors at the same spatial resolution as the emissions scaling factors, start to show the limitations of this method when we cannot assume that the signatures are uniform over the whole country. When regional signatures prior means are within 50% of the current uncertainty in these signatures (e, k) the model is able to adjust these perturbed signatures back to their 'true' values with some success and correctly estimate FF and non-FF emissions over most of the UK. These results show some improvement on the methane only test (a, g), particularly for the lower magnitude FF sector, but there are some inaccuracies in emissions estimates in areas where sensitivity to emissions is lower, away from the HFD site in the south-east and IVG site in the north. When regional signatures prior means are perturbed further, and can lie anywhere within the full range of the current uncertainty in these signatures (f, l) posterior emissions estimates become more inaccurate than those from the methane-only model for the non-FF sector and show only minor improvements for the FF sector. When prior signatures are perturbed far from their true values, the model adjusts emissions rather than correcting the regional signatures, in order to produce modelled methane concentrations and modelled methane isotope ratios that best fit the observations. This result highlights the risks with including regional signatures with high uncertainties in the model; there is a large number of degrees of freedom and the model can adjust any of these parameters freely within prior uncertainties in order to produce the best fit to the observations. If emissions and signatures are not well constrained by the observations, this could lead to inaccurate emissions estimation.

Overall, these results suggest that accurate estimation of whole-UK FF and non-FF emissions could be possible when using δ^{13}C-CH_4 and δ^{2}H-CH_4 observations from the HFD and IVG sites, when regional signatures are well understood and have either no or only minor spatial variation. However, even when uncertainty in regional signatures is low, careful consideration of the model's sensitivity to emissions from different regions is important. Without this, undue certainty may be placed on results from the model in areas far from observation sites, where it is only able to replicate the methane-only model's potentially incorrect attribution of emissions. Importantly, these synthetic data tests used an idealised scenario with low model and observational uncertainties and consistently available high frequency observations. In a real-world scenario, extra care must be taken when using this method to estimate fluxes in areas of low sensitivity, which may be larger in reality when using filtered observations or higher observation and model errors.

3.2 UK methane emissions case study

The synthetic data test results presented above show that this inverse modelling method could potentially be used with methane isotope ratio observations to directly estimate sector-level UK methane emissions. However, this is an idealised scenario, which included no impact from background concentrations or emissions from western Europe, assumed accurate transport modelling and included observations from recently established or soon-to-be established sites which do not currently have the long history of observations required for this inverse modelling study.

To test these findings in a real-world scenario, we applied the inverse model to estimate monthly methane emissions from the FF and non-FF sectors from January 2022 to December 2023. We used δ^{13}C-CH_4 and δ^{2}H-CH_4 Boreas observations from HFD, alongside methane mole fraction observations from MHD, TAC, RGL, HFD, WAO and CBW. Three scenarios were tested: with regional signatures fixed at their prior means; with one signature per sector, which the model could adjust within

the prior PDFs; and one signature per sector per inversion grid cell (at the same resolution as the emissions scaling factors) which the model could adjust within the prior PDFs. These scenarios reflect those used in the synthetic data tests discussed above.

As Fig. 1 **(b)** shows, good sensitivity to emissions is limited to the south-east of the UK by the location of currently available observations. Therefore, we only estimate emissions and analyse results over this area of good sensitivity, where isotope ratio observations from HFD are most likely to be able to influence the model. This region is shown by the dashed black rectangle in Fig. 3, and is henceforth referred to as south UK (SUK).

All results are analysed relative to those from the methane-only inversion, in order to determine whether the additional observations provide greater constraint on FF and non-FF methane fluxes than a traditional single-gas inversion constrained by spatial information in the a priori emissions alone. Total emissions estimates from each sector are discussed in more detail below. First, the inverse model's ability to produce modelled isotope ratios is demonstrated.

Figure 5 shows posterior modelled methane model fractions and methane isotope ratios from the HFD site, from the test with regional signatures optimised at the same spatial resolution as the emissions scaling factors. Results are shown for five example months (August to December 2023) which are representative of the whole two-year case study. Comparison between observations (black) and modelled isotope ratios (purple) shows a good fit at most timestamps, other than when excursions away from baseline are extreme or when the measurement uncertainty (within a given 4 hour period, as discussed in section 2.3.1) is very large (as shown by error bars on the observations). Prior (grey) and posterior (blue or purple) modelled baselines are shown as solid lines. Histograms giving the difference between observed and modelled isotope ratios **(d,f)**) show how the model has effectively adjusted modelled isotope ratios away from their priors and closer to the observations. The model has adjusted both the boundary 'signatures' (as shown by adjustments in the baseline) and the methane emission and boundary condition scaling factors (as shown by a closer match between modelled isotope ratios and observations).

When using regional signatures fixed at their prior means, the residuals between modelled and observed isotope ratios increase in size, compared to when using variable regional signatures. Figure D1 shows that for δ^{13}C-CH_4, this is because the modelled isotope ratios have not moved significantly from their priors. The spread in difference between modelled and observed δ^2H-CH_4 decreases when using variable regional signatures, however even the model with fixed signatures shows some improvement on modelled δ^2H-CH_4, relative the the prior. The different impact of variable regional signatures on each type of methane isotope ratio could be due to the relative size of δ^{13}C-CH_4 and δ^2H-CH_4 excursions away from the baseline or could be due to the nature of the two observation types: δ^{13}C-CH_4 excursions away from the baseline can be either positive or negative depending on the source type, which could result in a baseline-like observed isotope ratio for times when a mixture of FF and non-FF sources impact the mole fraction. Whereas, δ^2H-CH_4 excursions away from the baseline are always negative, with the most negative values characteristic of biogenic (non-FF) sources. Smaller changes in FF and non-FF emissions scaling factors may therefore have a larger impact on the modelled δ^2H-CH_4 than the modelled δ^{13}C-CH_4.

Figure 6 shows each inversion model's posterior estimate of SUK FF and non-FF methane emissions for April-December 2023, when data availability from most sites was good. Similar results for 2022 are given in Fig. E1. Results for January-April 2023 are not shown as there were no methane isotope ratio observations available during that period. Within posterior

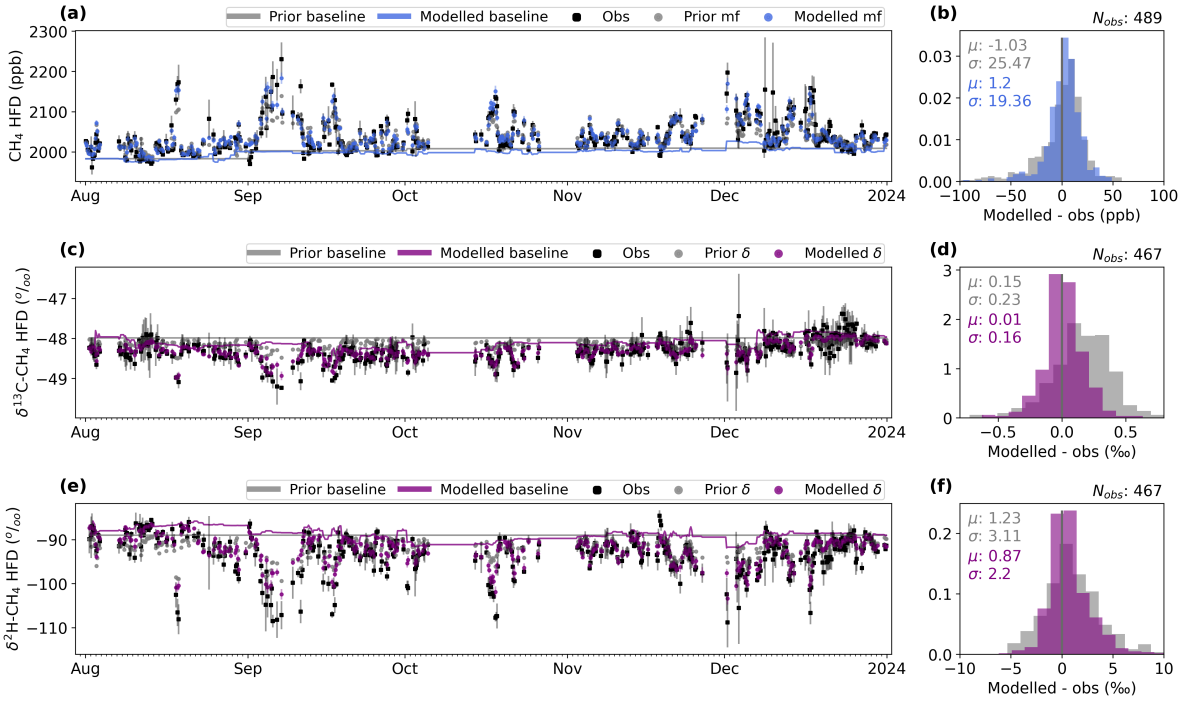

Figure 5. Modelled mole fractions and isotope ratios from the UK case study with methane isotope ratio observations from the HFD site and variable regional signatures, at the same spatial resolution as the emissions scaling factors. Four-hourly averaged observations (black squares) of CH_4 mole fractions **(a)**, δ^{13}C-CH_4 **(c)** and δ^{13}C-CH_4 **(e)** δ-values from the HFD site, for five example months August to December 2023. These are compared against posterior modelled values (darker colour) and prior modelled values (lighter colour) from the model with variable regional signatures. Differences between the observations and the prior (grey) and posterior (darker colour) modelled mole fractions and δ-values are given on the right, as histograms. The mean and standard deviations of these model-observation differences are also given. Prior (lighter line) and posterior (darker line) mean baselines are also shown for comparison.

uncertainties, there are no significant or consistent differences in the magnitude of posterior emissions estimates from either sector, between the methane-only model (blue bars) and the two models using methane isotope delta observations and uncertain source signatures (dark green and dark purple). Across the study period, mean SUK emissions estimates from these three model setups vary between 0.14 and 0.17 Tg/y for the FF sector and between 0.69 and 0.84 Tg/y for the non-FF sector. However, when using fixed source signatures (light purple bar), non-FF emissions estimates are in some cases up to 29% lower than the other three models, with a range of 0.49 to 0.82 Tg/y. This lowering of emissions from the non-FF sector is not coupled with an increase in FF emissions, so estimates of total emissions also decrease, within the high level of prior uncertainty in this two-sector inversion. This result highlights that care must be taken when assuming spatially and temporal invariant source signatures for source attribution. Due to the short time-series and limited data availability, we did not perform any trend or seasonal cycle analysis on these monthly emissions estimates.

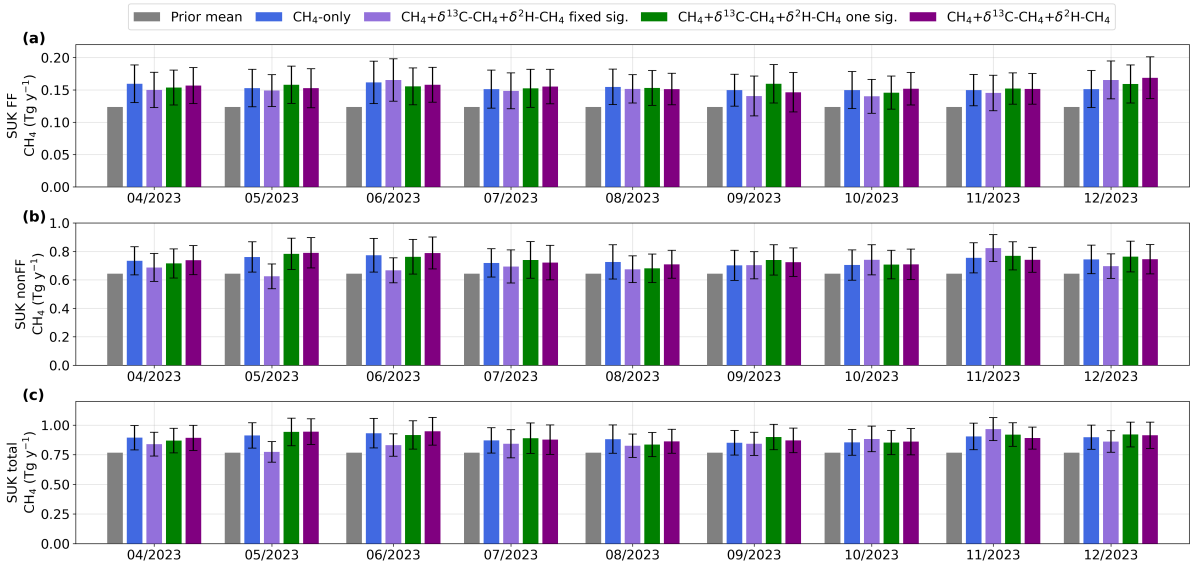

Figure 6. Posterior monthly April-December 2023 CH_4 flux estimates for the SUK area (as shown in Fig. 3) for the FF sector (a), non-FF sector (b) and all sources (c), for four different model setups. Results are given as a posterior mean (bar) and posterior 1-σ uncertainty. From left to right: prior mean (grey, where the large uncertainty is not shown), CH_4-only (blue); CH_4+δ^{13}C-CH_4+δ^2H-CH_4 with fixed regional signatures (light purple); CH_4+δ^{13}C-CH_4+δ^2H-CH_4 with one variable signature per sector (dark green) ;CH_4+δ^{13}C-CH_4+δ^2H-CH_4 with one variable signature per optimised cell per sector (dark purple).

There are no significant differences in posterior non-FF emissions uncertainty between results from the methane-only model and from the three models with different source signature setups. As a percentage of the posterior mean, 1-σ posterior uncertainty ranges from 23 to 34 % for the non-FF sector for all models. However, the range of posterior uncertainties in FF emission estimates is slightly wider from the model with fixed source signatures (between 29 to 46 %) compared to posterior FF uncertainties from the other three models (between 31 and 43 %). A relatively high uncertainty is to be expected from the methane-only model, where only the spatial distribution and magnitude of emissions in the prior provide constraint on the posterior sector split, which leads to a range of possible magnitudes of FF and non-FF emissions which satisfy the methane concentration's constraint on total methane emissions. The isotope ratio observations' lack of impact on posterior uncertainty is discussed in more detail in Section 4.

Mean average spatial emissions estimates from all model setups for April-December 2023 are given in Fig. 7. Emissions from the methane-only inversion are given relative to the prior mean emission for the FF **(a)** and non-FF sector **(e)**. Emission estimates from the models with secondary observations are given as differences from the methane-only model, to better show the minor differences in results. On average across this period, the methane-only model slightly increased FF emissions across the SUK area, relative to the prior. The models with variable signatures **(c,d)** on average show little difference in FF emissions estimates, relative to the methane-only model. When using fixed signatures **(b)**, there is a small reduction in posterior FF

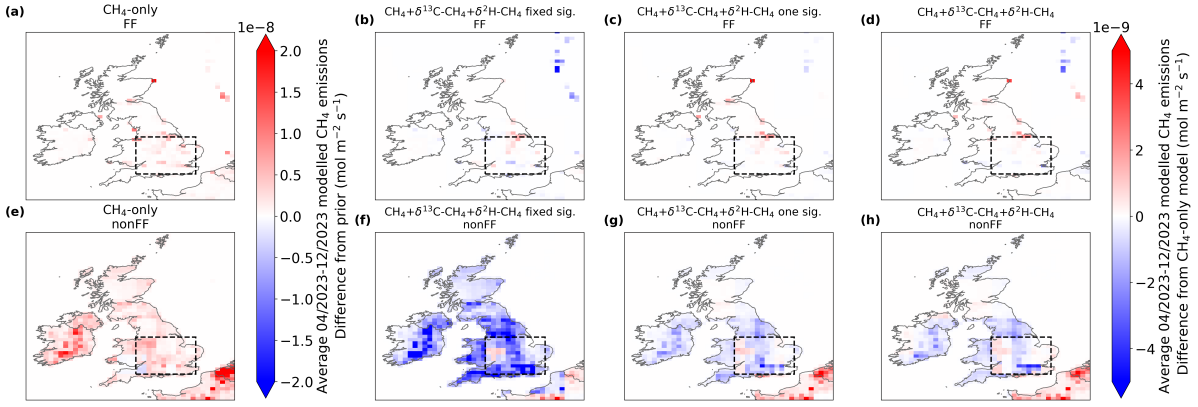

Figure 7. Average posterior mean monthly flux estimates for UK across April-December 2024 for the FF sector (top row) and non-FF sector (bottom row) from all model setups. Dashed lines show the SUK area, over which results are analysed. From left to right: CH_4-only; CH_4+δ^{13}C-CH_4+δ^2H-CH_4 with fixed regional signatures; CH_4+δ^{13}C-CH_4+δ^2H-CH_4 with one signature per sector; CH_4+δ^{13}C-CH_4+δ^2H-CH_4 with one signature per optimised region per sector. CH_4-only results are given as absolute differences from the prior emissions estimates. Results from all other models are given as absolute differences from this CH_4 posterior-prior difference.

emissions in the south of the SUK region, countered by an increase in the north, relative to the methane-only model. For the non-FF sector, the methane-only model produces a general upward scaling of emissions relative the prior. With variable regional signatures **(g,h)** the models suggest a reduction of non-FF emissions in south-east England, close to London and to the HFD site, relative to the methane-only model. With fixed signatures there is strong negative scaling of non-FF emissions across most of the SUK area. As noted previously, the model with fixed signatures produces a poor fit to the isotope ratio observations; these results show that the model may be scaling down non-FF emissions, which have more negative signatures, in order to improve this fit. This shows that a dependence on fixed source signatures could potentially lead to unrealistic estimates of emissions.

Beyond the SUK area, adjustments to emissions are only minor when using variable signatures, compared to results from the methane-only model. This result may change as the network of isotope ratio observations expands in the near future, and further work will be carried out to test the impact of these observations on whole-UK FF and non-FF emissions, when using uncertain source signatures.

Table 3 gives the posterior signatures from both models with variable signatures, as averages from all inversion months. We found no spatial or temporal trends in posterior signatures across the SUK region, therefore results are presented as average means and minimums and maximums of posterior signature PDFs for all cells within the SUK area (for the model with one signature per region). Posterior uncertainty in signatures remains high, although there is some reduction relative to the prior uncertainty (see Table 2). This narrowing of posterior signature uncertainty suggests that signatures at the more extreme ends of the prior PDFs are not required in order to produce a good fit to observations, in a model at this spatial resolution where most regions contain a mixture of sources with a combined less-extreme signature. We also found no relationship between posterior

	FF regional signatures (‰)	non-FF regional signatures (‰)	Boundary 'signatures' (‰)
δ^{13}C-CH_4 one value per sector	-40.0 (-42.8, -37.0)	-59.7 (-66.3, -52.1)	-48.0 (-49.1, -47.1)
δ^{13}C-CH_4 one value per region	-40.0 (-43.1, -36.7)	-59.8 (-66.8, -51.7)	-48.0 (-49.1, -47.1)
δ^{2}H-CH_4 one value per sector	-159.5 (-169.7, -149.3)	-283.0 (-329.0, -245.1)	-88.4 (-98.9, -77.1)
δ^{2}H-CH_4 one value per region	-159.7 (-170.1, -149.4)	-280.5 (-303.3, -259.5)	-88.5 (-98.1, -77.2)

Table 3. Average source and boundary signatures from the two models with variable signatures. Results are given as the mean posterior signature across all inversion months and the minimum and maximum of the posterior PDFs across all inversion months, to show the full uncertainty in these values. For the model with one signature per sector per region, posterior PDFs are only included for regions within the SUK area.

mean signatures and posterior mean emission scaling factors (see Fig. F1) across the SUK area, which shows that emissions estimates are not being strongly biased by adjustments to the signatures. However, this result and the wide range of posterior regional signatures produced by the inversions suggests that the model may be adjusting regional signatures within their prior uncertainties, to produce modelled isotope ratios with a better fit to the observed isotope ratios, rather than adjusting emissions. Posterior boundary 'signatures' are similar for both model setups, as expected, and generally the lowest boundary signatures were estimated for the southern boundary of the inversion domain.

4 Discussion

This case study has shown that using the inverse model with uncertain source signatures and methane isotope ratio observations from one site produces estimates of SUK FF and non-FF emissions with no significant differences when compared to results from a methane-only inverse model. This could be due to a range of factors. Firstly, the prior estimate of emissions from each sector could be accurate, in terms of producing modelled mole fractions and isotope ratios which produce a good fit to atmospheric observations. If this was the case, additional information from the isotope ratio observations would not impact the model's emissions estimates, relative to what the methane-only model achieves. Alternatively, the isotope ratio observations may not be able to provide any greater constraint on emissions because there is a relative lack of information from the isotope observations (from only one site) compared to that from the mole fraction observations (six sites) and uncertainties from the constraining parameters (source signatures) may be too high.

The synthetic data test showed that the model was most effective at estimating FF and non-FF emissions with uncertain regional signatures when there was only one signature per emissions sector. However, this case study has shown that in a real-world test of this scenario, results from the model are similar to those from the methane-only model. This could suggest that in reality there is some spatial variation in source signatures which cannot be captured by this model setup, and therefore this restriction is limiting the additional observations' ability to impact posterior emissions uncertainty. The synthetic data tests also used isotope ratio observations from two sites, compared to the single site used for the UK case study. To compensate for this,

we analysed the case study results over the SUK region where the HFD site should have good sensitivity to emissions. However, results over this region do not vary significantly from those from the methane-only model (as discussed in detail above), potentially suggesting that more isotope ratio observations are required to provide enough information to better constrain sector-level emissions across any area of the UK.

Previous work showed that incorporating ethane observations ~~in~~ into the inversion was a more effective method of reducing the model's uncertainty in posterior FF fluxes (Ramsden et al., 2022). Ethane's greater impact on FF flux uncertainty could be due to a range of factors: higher density of ethane observations, location of these ethane observations in relation to sensitivity to UK-wide emissions, or lower uncertainty in ethane:methane emission ratios, compared to the uncertain regional signatures included in this work. Combining both ethane and methane isotope ratio observations in the inversion could provide greater constraint on emissions, even despite the increased prior uncertainties involved with including additional observations and ethane:methane emission ratios. This will be explored in future work with this method.

The nature of methane isotope source signatures, compared to ethane:methane emission ratios, may also be limiting the model's ability to use the additional information from methane isotope ratio observations to reduce regional posterior flux uncertainty. In this work, emissions are optimised on a regional scale, with emissions originating from a range of sources inside each optimised grid cell area. As discussed above, the resulting isotopic source signature from each cell will be an average from all these sources (a 'regional signature'), which may potentially reduce the size of any excursions away from the background signature seen in the observations of this area. This therefore reduces the information available from the methane isotope ratio observations. This is different from the use of ethane observations, which includes an inference of a methane FF source in an optimised grid cell simply if there are also ethane emissions originating from that area.

Improved understanding of methane isotope source signatures, or improved incorporation of our current understanding into the model, is also a key focus for future developments in this field. Currently, this model assumes a two-sector setup with a large uncertainty in source signatures from the non-FF sector and no spatial information in the source signature priors. However, information on the spatial distribution of agriculture and waste sources (which both contribute to the non-FF sector) could potentially be used to produce a non-FF signature prior with spatial information, to better inform the modelled isotope ratios and reduce prior uncertainty in some regions. Alternatively, a three-sector inversion could be carried out, using the assumption that the agriculture and waste sectors have distinct source signatures. Using this assumption, this method could potentially assign emissions inaccurately to each of the agriculture or waste sectors, but produce FF emissions estimates with lower uncertainty. Currently, we assume no spatial or temporal correlations in emissions or source signatures. Inclusion of these correlations could limit the model from over-adjusting signatures locally, where it is assumed that emissions sources will be similar, and might allow for greater constraint on emissions.

Without greater understanding of isotopic source signatures and a higher density network of isotope observations, the added complexity involved with using isotope ratio observations and uncertain source signatures may limit this method from providing accurate high-resolution information about spatial distributions of FF and non-FF fluxes on a regional scale.

5 Conclusions

This work has presented a novel inverse modelling method that is highly adaptable and can be used with range of secondary observations to directly estimate emissions from two (or more) sectors concurrently. The model uses the relationship between observations of its primary gas (in this case methane) to secondary isotope ratio observations, via regional isotopic signatures, to produce posterior flux estimates with an aim to reduce posterior uncertainty, relative to traditional methane inverse modelling methods. This works builds on previous methods using isotope ratio observations for source attribution, by considering both the uncertainties and spatial and temporal differences in isotopic source signatures.

Using synthetic data tests, we showed that the inverse model can use methane isotope ratio observations to accurately estimate UK methane emissions from both FF and non-FF sectors, considering a range of scenarios with different uncertainties on the methane isotope regional signatures. The model performed best when regional isotopic signatures were well understood or had low uncertainty. In high-uncertainty scenarios, emission estimates were less accurate than the methane-only model.

The inverse method was used with new δ^{13}C-CH_4 and δ^{2}H-CH_4 observations from the Heathfield (HFD) site in southern England, to estimate monthly FF and non-FF methane fluxes for a region in the south-east UK, between 2022 and 2023. Over this study period, the inverse model with methane isotope ratio observations produced similar estimates of FF and non-FF emissions to those from the methane-only model. This suggests that this combination of limited UK methane isotope ratio observations and high uncertainties in isotopic source signatures is preventing these observations from providing further constraint on emissions. However, this observational network is currently expanding to include additional methane isotope ratio observations, which may improve the viability of this method for producing FF and non-FF methane emissions estimates with reduced uncertainty, relative to the methane-only model.

The use of secondary observations for source attribution of methane emissions during top-down emissions estimation is a key research target for many current projects, including two Horizon Europe research projects: the Process Attribution of Regional Emissions (PARIS) project and the Metrology for European emissions verification on methane isotopes (isoMET) project. These projects include a focus on expanding European networks of methane isotope ratio and ethane observations and improving our understanding of the source signatures of methane's sources. Work presented here shows that with this continued investment in reliable long-term networks of secondary observations, this inverse modelling method could potentially be used to provide an independent verification of the UK and Europe's bottom-up flux estimates at a broad-sector level. This independence will become a key component of effectively monitoring trends in the UK and Europe's methane emissions in the future, as emissions targets and reporting requirements become more stringent.

Code and data availability. Methane mole fraction data for Mace Head, Weybourne, Tacolneston, Bilsdale, Ridge Hill and Heathfield are available through the ICOS Carbon Portal, DOI: 10.18160/46ST-DEVK (ICOS RI et al., 2025). Measurements of methane isotope ratio from HFD are also available through the ICOS Carbon Portal, PID: 11676/MRHwmQFqm0O_Y39065JsIQLS (Rennick et al., 2025) NOAA MHD flask measurements of δ^{13}C-CH_4 are available from https://gml.noaa.gov/aftp/data/trace_gases/ch4c13/flask/surface/ (last access 4 March 2025). The NAME III v7.2 transport model is available from the UK Met Office under licence by contacting enquiries@metoffice.gov.uk.

The meteorological data used to drive the transport model from the UK Met Office operational Numerical Weather Prediction (NWP) Unified Model (UM) are available from https://catalogue.ceda.ac.uk/uuid/78f23c539d304591b137cf986b69a525/ and https://catalogue.ceda.ac.uk/uuid/e4ac04e7fa2541278ad4ad06fb4fd5f3/ (last access 4 March 2025). The UK Greenhouse Gas (UKGHG) model is available from https://github.com/NERC-CEH/ukghg (last access 4 March 2025). The EDGAR v8.0 methane inventory is available from https://edgar.jrc.ec.europa.eu/dataset_ghg80 (last access 25 September 2025). The code used to run the inverse model and estimate methane emissions using these data products is available from https://doi.org/10.5281/zenodo.18496508 (Ramsden, 2026).

Appendix A: Calculating isotopologue absolute fractions

This method assumes that there are only three methane isotopologues present in the atmosphere: $^{12}CH_4$, $^{13}CH_4$ and $^{12}CH_3D$. The total methane mole fraction can be found by summing the contributions from each isotopologue:

$$CH_4 = {}^{12}CH_4 + {}^{13}CH_4 + {}^{12}CH_3D \tag{A1}$$

The absolute mole fraction of each isotopologue can be found by considering the ratio of isotopologues given by isotope ratio observations and substituting this information into Equation A1.

Methane isotope ratio observations are presented as delta values:

$$\delta_i = \left(\frac{R_i}{R_{std_i}} - 1 \right) \times 1000 \tag{A2}$$

where R_i for the two sets of methane isotope observations used in this work are:

$$R_{13} = \frac{^{13}CH_4}{^{12}CH_4} \tag{A3}$$

$$R_2 = \frac{^{12}CH_3D}{^{12}CH_4} \tag{A4}$$

To find the absolute fraction of $^{12}CH_4$:

Equations A3 and A4 are rearranged then substituted into A1:

$$\begin{aligned}
{}^{13}CH_4 &= {}^{12}CH_4 R_{13} \\
{}^{12}CH_3D &= {}^{12}CH_4 R_2 \\
CH_4 &= {}^{12}CH_4 + {}^{12}CH_4 R_{13} + {}^{12}CH_4 R_2 \\
CH_4 &= {}^{12}CH_4 (1 + R_{13} + R_2) \\
{}^{12}CH_4 &= \frac{CH_4}{(1 + R_{13} + R_2)}
\end{aligned} \tag{A5}$$

Similarly for $^{13}CH_4$ and $^{12}CH_3D$:

$$
\begin{aligned}
{}^{12}\mathrm{CH_4} &= \frac{{}^{13}\mathrm{CH_4}}{R_{13}} \\
{}^{12}\mathrm{CH_3D} &= {}^{12}\mathrm{CH_4} R_2 \\
\mathrm{CH_4} &= \frac{{}^{13}\mathrm{CH_4}}{R_{13}} + {}^{13}\mathrm{CH_4} + {}^{12}\mathrm{CH_4} R_2 \\
\mathrm{CH_4} &= \frac{{}^{13}\mathrm{CH_4}}{R_{13}} + {}^{13}\mathrm{CH_4} + \frac{{}^{13}\mathrm{CH_4}}{R_{13}} R_2 \\
\mathrm{CH_4} &= {}^{13}\mathrm{CH_4} \left(\frac{1}{R_{13}} + 1 + \frac{R_2}{R_{13}} \right) \\
{}^{13}\mathrm{CH_4} &= \frac{\mathrm{CH_4}}{\left(1 + \frac{1}{R_{13}} + \frac{R_2}{R_{13}} \right)}
\end{aligned}
\tag{A6}
$$

$$
\begin{aligned}
{}^{13}\mathrm{CH_4} &= {}^{12}\mathrm{CH_4} R_{13} \\
{}^{12}\mathrm{CH_4} &= \frac{{}^{12}\mathrm{CH_3D}}{R_2} \\
\mathrm{CH_4} &= \frac{{}^{12}\mathrm{CH_3D}}{R_2} + {}^{12}\mathrm{CH_4} R_{13} + {}^{12}\mathrm{CH_3D} \\
\mathrm{CH_4} &= \frac{{}^{12}\mathrm{CH_3D}}{R_2} + \frac{{}^{12}\mathrm{CH_3D}}{R_2} R_{13} + {}^{12}\mathrm{CH_3D} \\
\mathrm{CH_4} &= \frac{{}^{12}\mathrm{CH_3D}}{\frac{1}{R_2} + \frac{R_{13}}{R_2} + 1} \\
{}^{12}\mathrm{CH_3D} &= \frac{\mathrm{CH_4}}{\left(1 + \frac{1}{R_2} + \frac{R_{13}}{R_2} \right)}
\end{aligned}
\tag{A7}
$$

These terms can then used to produce modelled atmospheric methane isotope ratios as described in Section 2.2.

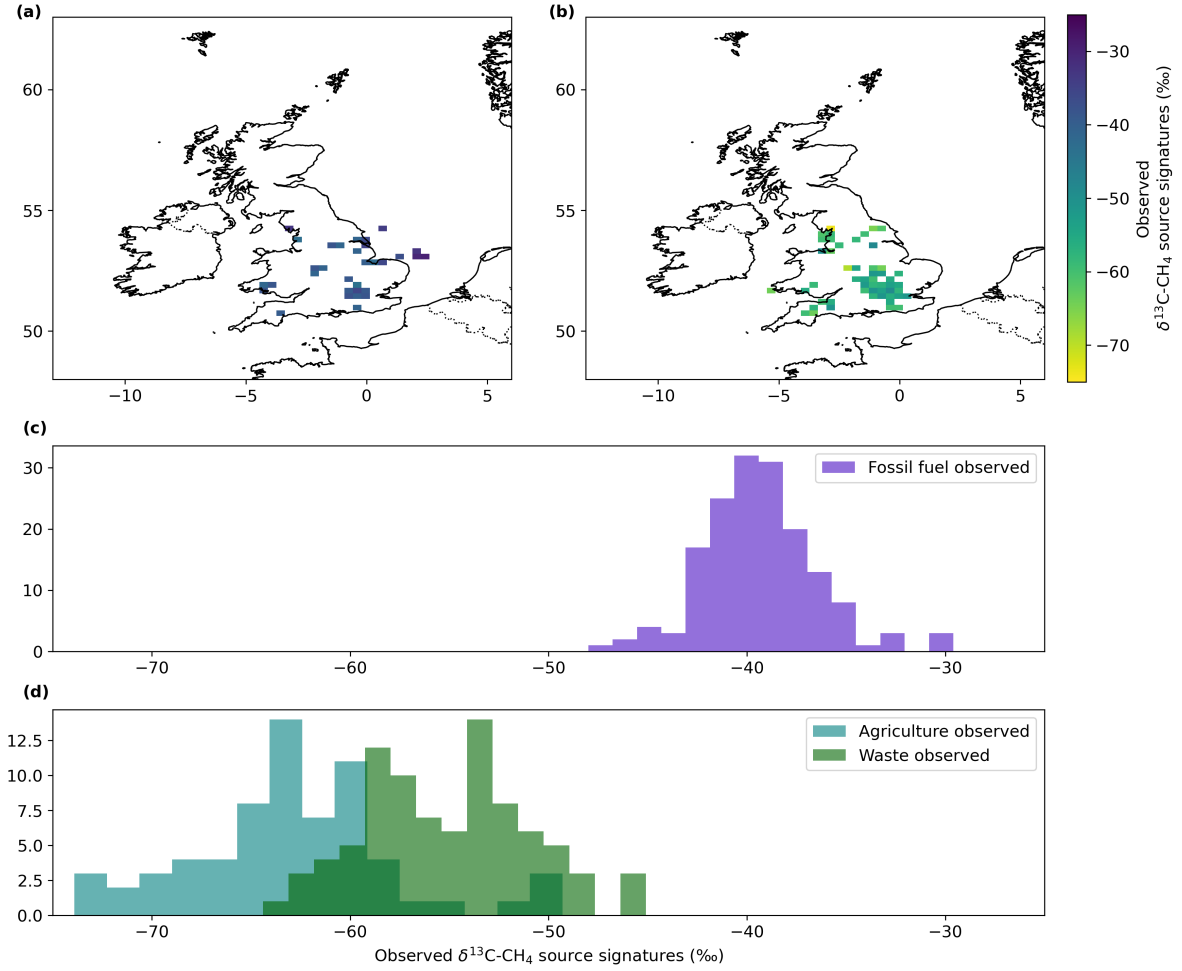

Figure A1. δ^{13}C-CH$_4$ point source signatures compiled during the isoMET project (Dasgupta et al., 2025a, b) and observed by Royal Holloway during ground-based observation campaigns (Lowry et al., 2020; Menoud et al., 2022) from FF **(a,c)** and non-FF **(b,d)** sources. Point source signatures have been averaged spatially and temporally to the 25 km resolution of the atmospheric transport model used in this study **(a,b)**. The values are also presented as histograms **(c,d)** with non-FF sources split into agriculture (light blue) and waste (green) sources, showing the overlap between these two sectors.

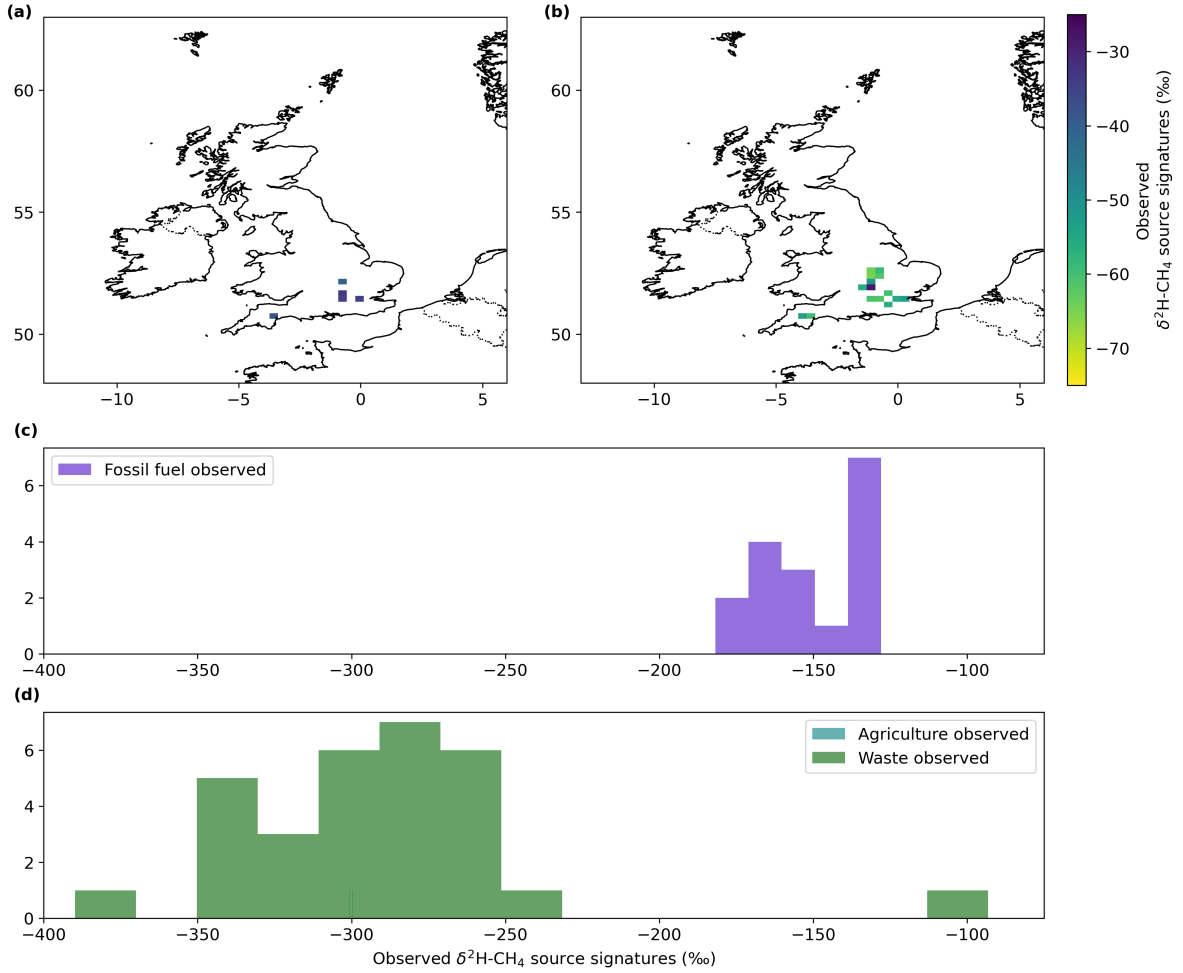

Figure B1. δ^2H-CH$_4$ point source signatures compiled during the isoMET project (Dasgupta et al., 2025a, b) from FF **(a,c)** and non-FF **(b,d)** sources. Point source signatures have been averaged spatially and temporally to the 25 km resolution of the atmospheric transport model used in this study **(a,b)**. The values are also presented as histograms **(c,d)**. Only values for the waste sector (green) are shown in the histogram, due to the lack of data for agriculture.

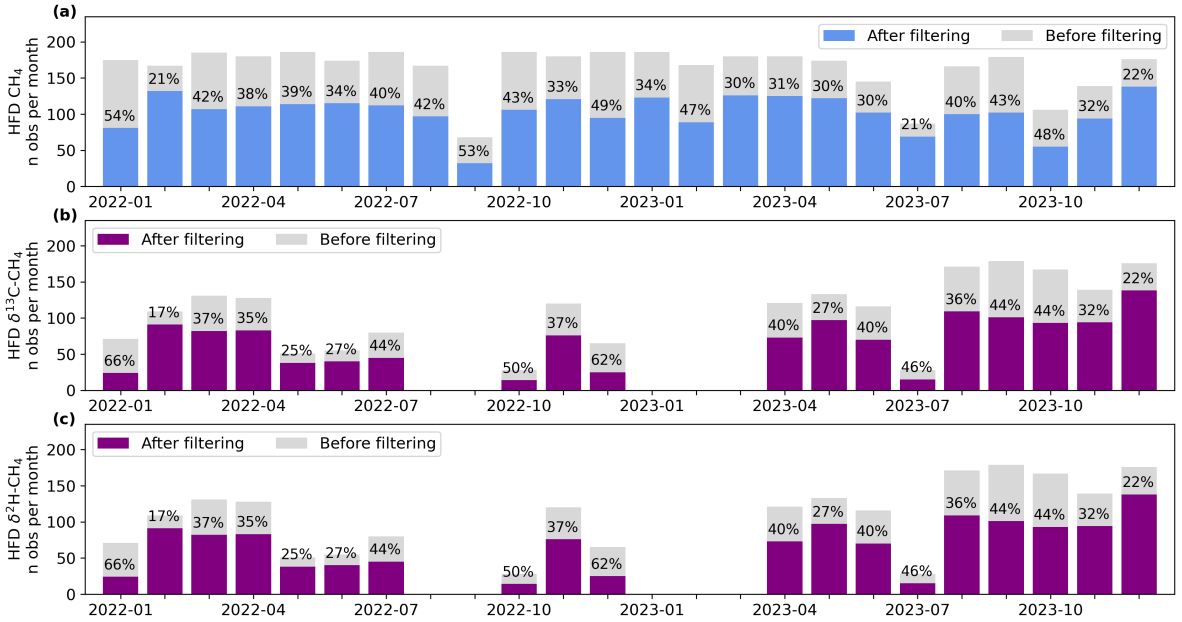

Figure C1. Number of 4-hourly averaged observations available from the Heathfield (HFD) site for each monthly inversion period before filtering (grey) and after filtering (coloured bar), for methane (a), δ^{13}C-CH_4 (b) and δ^{2}H-CH_4 (c). Annotated values give the percentage of observations that were removed by filtering based on meteorological conditions (see 2.3.1 for more information on this filtering).

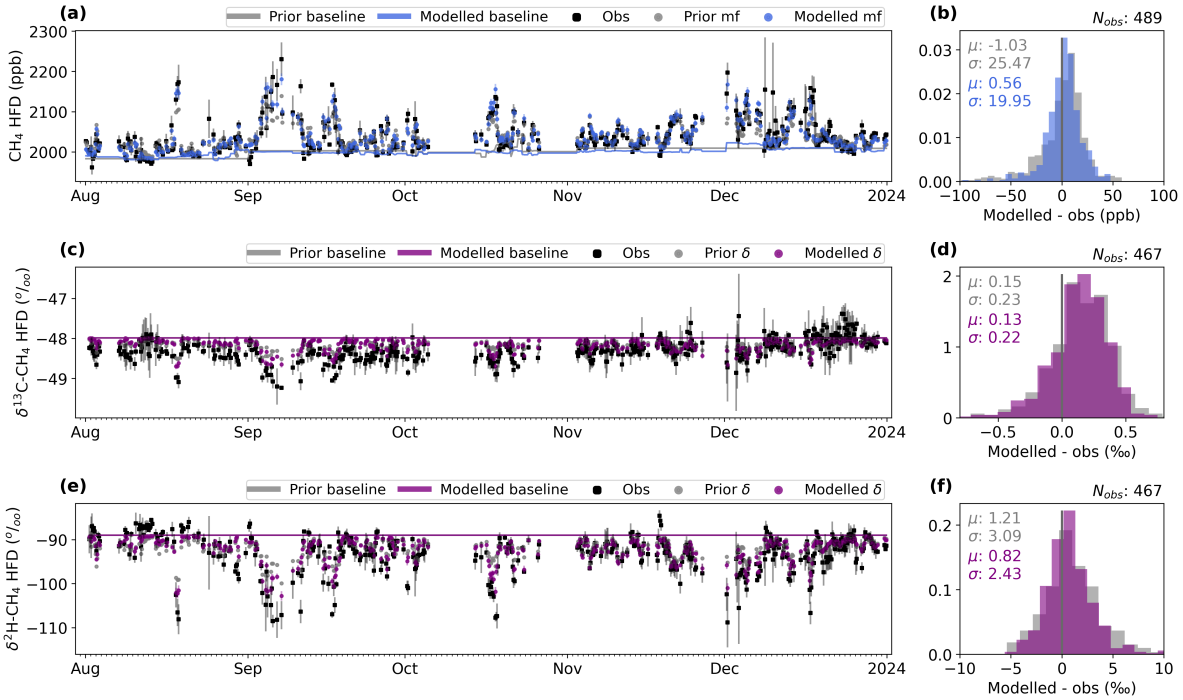

Figure D1. Modelled methane mole fractions and isotope ratios from the UK case study with methane isotope ratio observations from the HFD site and fixed regional signatures. Four-hourly averaged observations (black squares) of CH_4 mole fractions **(a)**, δ^{13}C-CH_4 **(b)** and δ^{13}C-CH_4 **(c)** δ-values from the HFD site, for five example months August to December 2023. These are compared against posterior modelled values (darker colour) and prior modelled values (lighter colour) from the model with fixed source signatures. Differences between the observations and the prior (grey) and posterior (darker colour) modelled mole fractions and δ-values are given on the right, as histograms. The mean and standard deviations of these model-observation differences are also given. Prior (lighter line) and posterior (darker line) mean baselines are also shown for comparison. For these model runs with fixed source signature terms, the prior and posterior baselines are identical for the isotope ratio terms.

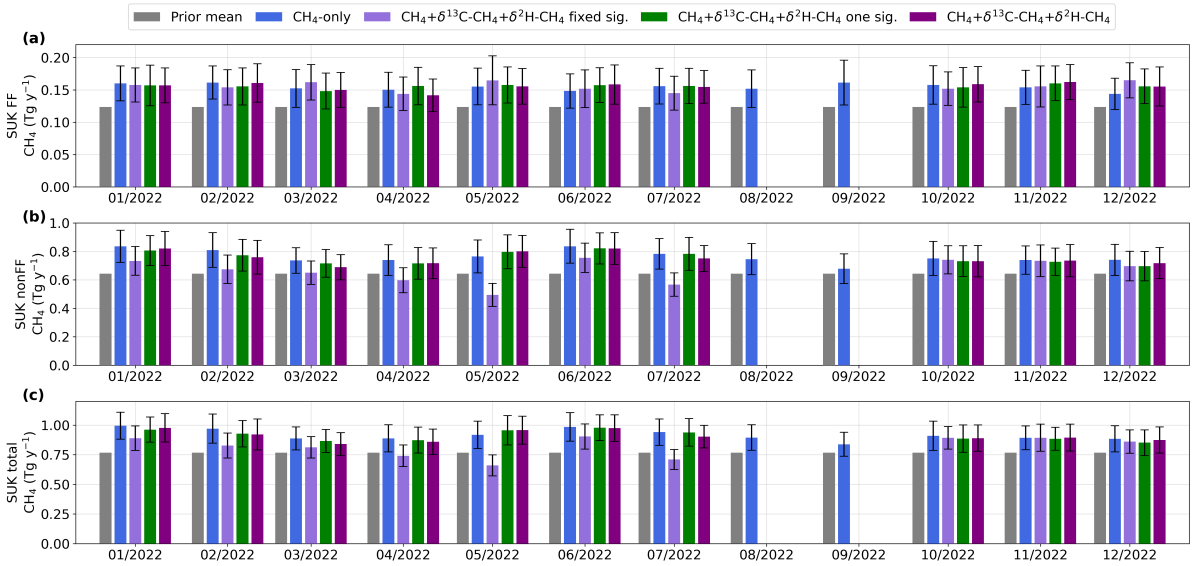

Figure E1. Posterior monthly 2022 CH_4 flux estimates for the SUK area (as shown in Fig. 3) for the FF sector (a), non-FF sector (b) and all sources (c), for four different model setups. Results are given as a posterior mean (bar) and posterior 1-σ uncertainty. From left to right: prior mean (grey, where the large uncertainty is not shown), CH_4-only (blue); CH_4+δ^{13}C-CH_4+δ^2H-CH_4 with fixed regional signatures (light purple); CH_4+δ^{13}C-CH_4+δ^2H-CH_4 with one variable signature per sector (dark green) ;CH_4+δ^{13}C-CH_4+δ^2H-CH_4 with one variable signature per optimised cell per sector (dark purple)

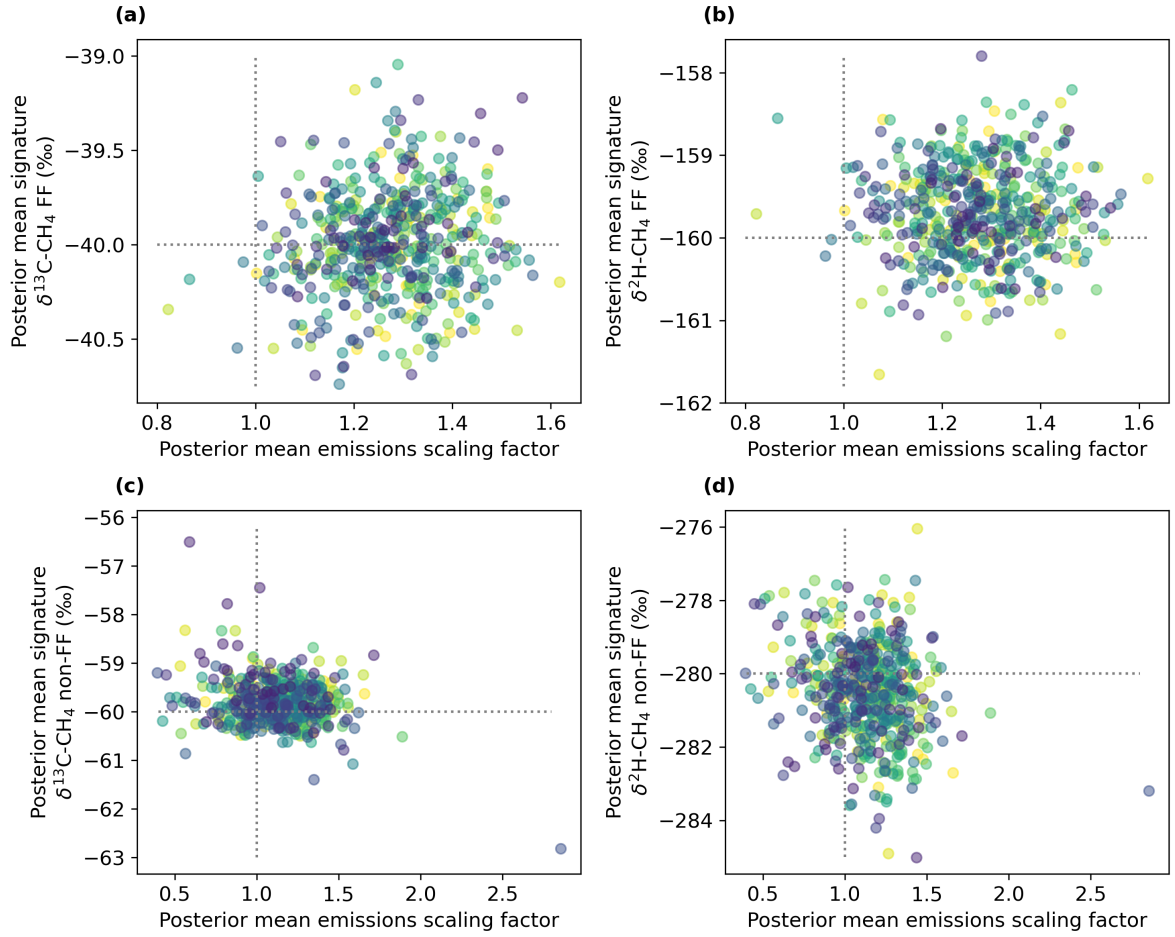

Figure F1. Posterior mean regional signature from the inverse model with one signature per inversion grid cell (y axis), compared to the posterior mean emissions scaling factor (x axis) from the same grid cell. Shown for δ^{13}C-CH_4 FF **(a)**, δ^{2}H-CH_4 FF **(b)**, δ^{13}C-CH_4 non-FF **(c)** and δ^{2}H-CH_4 non-FF **(d)**. Different colours represent different monthly inversions.

Author contributions. AR and AG led the method development, code development and investigation. AR led the manuscript preparation. CR, TA, ES, DF, and CY developed the Boreas isotope instrument, provided these observations and contributed to method development. EC contributed to method development. AM provided NAME footprints and advised on the study. M Rigby advised on the study. DL provided methane isotope source signature measurements. PL provided the UKGHG methane flux model. KS, SO, DY and JP made the measurements from the UK DECC network. DM, ML and M Ramonet provided measurements from MHD. GF provided measurements from WAO. AF provided measurements from CBW. All co-authors contributed to review of the manuscript, with significant contributions from AG, M Rigby, JP, CR and TA.

Competing interests. The authors declare that they have no conflicts of interest.

Acknowledgements. Alice E. Ramsden was supported by the Met Office Hadley Centre Climate Programme (funded by the UK Department for Science Innovation and Technology (DSIT)) and the Greenhouse Gas Emissions Measurement and Modelling Advancement (GEMMA) Programme (funded by NERC and the UKRI Building a Green Future theme (E/Y001788/1)). Anita L. Ganesan and Matt Rigby were supported by the PARIS (Process Attribution of Regional Emissions) project, which was funded by the UK Innovate (10043720, University of Bristol, 10070687, Met Office) and Horizon EU (101081430) grants. Measurements from the UK Deriving Emissions linked to Climate Change (DECC) Network were funded by the UK Department for Energy Security and Net Zero (DESNZ) through contracts numbers TRN1028/06/2015, TRN1537/06/ 2018, TRN5488/11/2021 and prj_1604 to the University of Bristol. Measurements at Heathfield (HFD) are maintained by the National Physical Laboratory under funding from the National Measurement System by UK DSIT. The HFD Boreas methane isotope observations were supported by the European Partnership on Metrology (EURAMET) 21GRD04 isoMET project, co-financed from the European Union's Horizon Europe Research and Innovation Programme and by the Participating States. The authors would like to thank the ICOS Atmospheric Thematic Centre, Central Calibration Laboratory and Carbon Portal for providing the facilities used to collect, process and distribute the measurement data used in this study. This work was carried out using the computational facilities of the Advanced Computing Research Centre at the University of Bristol and the Azure SPICE facilities at the Met Office. We would like to thank those that have contributed to the Bristol Atmospheric Chemistry Research Group's code repository.

References

Arias, P., Bellouin, N., Coppola, E., Jones, R., Krinner, G., Marotzke, J., Naik, V., Palmer, M., Plattner, G.-K., Rogelj, J., Rojas, M., Sillmann, J., Storelvmo, T., Thorne, P., Trewin, B., Achuta Rao, K., Adhikary, B., Allan, R., Armour, K., Bala, G., Barimalala, R., Berger, S., Canadell, J., Cassou, C., Cherchi, A., Collins, W., Collins, W., Connors, S., Corti, S., Cruz, F., Dentener, F., Dereczynski, C., Di Luca, A., Diongue Niang, A., Doblas-Reyes, F., Dosio, A., Douville, H., Engelbrecht, F., Eyring, V., Fischer, E., Forster, P., Fox-Kemper, B., Fuglestvedt, J., Fyfe, J., Gillett, N., Goldfarb, L., Gorodetskaya, I., Gutierrez, J., Hamdi, R., Hawkins, E., Hewitt, H., Hope, P., , Islam, A., Jones, C., Kaufman, D., Kopp, R., Kosaka, Y., Kossin, J., S., K., Lee, Y.-Y., Li, J., Mauritsen, T., Maycock, T., Meinshausen, M., Min, S.-K., Monteiro, P., Ngo-Duc, T., Otto, F., Pinto, I., Pirani, A., Raghavan, K., Ranasinghe, R., Ruane, A., Ruiz, L., Sallée, J.-B., Samset, B., Sathyendranath, S., Seneviratne, S., Sörensson, A., Szopa, S., Takayabu, I., Tréguier, A.-M., van den Hurk, B., R., V., von Schuckmann, K., Zaehle, S., Zhang, X., and Zickfeld, K.: Technical Summary. In Climate Change 2021: The Physical Science Basis. Contribution of Working Group I to the Sixth Assessment Report of the Intergovernmental Panel on Climate Change, Tech. rep., Intergovernmental Panel on Climate Change, Cambridge, United Kingdom and New York, NY, USA, https://doi.org/10.1017/9781009157896.002, 2021.

AVENGERS: Attributing and Verifying European and National Greenhouse Gas and Aerosol Emissions and Reconciliation with Statistical Bottom-up Estimates (AVENGERS), https://avengers-project.eu/, 2023.

Bakkaloglu, S., Lowry, D., Fisher, R. E., France, J. L., and Nisbet, E. G.: Carbon isotopic characterisation and oxidation of UK landfill methane emissions by atmospheric measurements, Waste Management, pp. 162–175, https://doi.org/10.1016/j.wasman.2021.07.012, 2021.

Barkley, Z. R., Davis, K. J., Feng, S., Cui, Y. Y., Fried, A., Weibring, P., Richter, D., Walega, J. G., Miller, S. M., Eckl, M., Roiger, A., Fiehn, A., and Kostinek, J.: Analysis of Oil and Gas Ethane and Methane Emissions in the Southcentral and Eastern United States Using Four Seasons of Continuous Aircraft Ethane Measurements, J. Geophys. Res.-Atmos., 126, https://doi.org/10.1029/2020JD034194, 2021.

Basu, S., Lan, X., Dlugokencky, E., Michel, S., Schwietzke, S., Miller, J. B., Bruhwiler, L., Oh, Y., Tans, P. P., Apadula, F., Gatti, L. V., Jordan, A., Necki, J., Sasakawa, M., Morimoto, S., Di Iorio, T., Lee, H., Arduini, J., and Manca, G.: Estimating emissions of methane consistent with atmospheric measurements of methane and δ^{13}C of methane, Atmos. Chem. Phys., 22, 15 351–15 377, https://doi.org/10.5194/acp-22-15351-2022, 2022.

Brand, W. A., Assonov, S. S., and Coplen, T. B.: Correction for the 17O interference in δ(13C) measurements when analyzing CO2 with stable isotope mass spectrometry (IUPAC Technical Report), Pure Appl. Chem., 82, 1719–1733, https://doi.org/10.1351/PAC-REP-09-01-05, 2010.

Cain, M., Warwick, N. J., Fisher, R. E., Lowry, D., Lanoisellé, M., Nisbet, E. G., France, J., Pitt, J., O'Shea, S., Bower, K. N., Allen, G., Illingworth, S., Manning, A. J., Bauguitte, S., Pisso, I., and Pyle, J. A.: A cautionary tale: A study of a methane enhancement over the North Sea, J. Geophys. Res.-Atmos., 122, 7630–7645, https://doi.org/10.1002/2017JD026626, 2017.

Cui, Y. Y., Henze, D. K., Brioude, J., Angevine, W. M., Liu, Z., Bousserez, N., Guerrette, J., McKeen, S. A., Peischl, J., Yuan, B., Ryerson, T., Frost, G., and Trainer, M.: Inversion Estimates of Lognormally Distributed Methane Emission Rates From the Haynesville-Bossier Oil and Gas Production Region Using Airborne Measurements, J. Geophys. Res.-Atmos., 124, 3520–3531, https://doi.org/10.1029/2018JD029489, 2019.

Dasgupta, B., Menoud, M., Van Der Veen, C., Levin, I., Veidt, C., Moossen, H., Englund Michel, S., Sperlich, P., Morimoto, S., Fujita, R., Umezawa, T., Platt, S., Zwaaftink, C. G., Myhre, C. L., Fisher, R., Lowry, D., Nisbet, E. G., France, J., Woolley Maisch, C., Brailsford, G., Moss, R., Goto, D., Pandey, S., Houweling, S., Warwick, N., and Röckmann, T.: Harmonisation of methane isotope ratio measurements

from different laboratories using atmospheric samples, Atmos. Meas. Tech., 18, 6591–6607, https://doi.org/10.5194/amt-18-6591-2025, 2025a.

Dasgupta, B., Menoud, M., Van Der Veen, C., Levin, I., Veidt, C., Moossen, H., Englund Michel, S., Sperlich, P., Morimoto, S., Fujita, R., Umezawa, T., Platt, S., Zwaaftink, C. G., Myhre, C. L., Fisher, R., Lowry, D., Nisbet, E. G., France, J., Woolley Maisch, C., Brailsford, G., Moss, R., Goto, D., Pandey, S., Houweling, S., Warwick, N., and Röckmann, T.: Harmonised and offset corrected methane isotopic composition (ch4, 13ch4, d2h_ch4) from high northern and southern latitudes, https://doi.org/10.18160/V1Y4-NTK0, 2025b.

Drinkwater, A., Palmer, P. I., Feng, L., Arnold, T., Lan, X., Michel, S. E., Parker, R., and Boesch, H.: Atmospheric data support a multi-decadal shift in the global methane budget towards natural tropical emissions, Atmos. Chem. Phys., 23, 8429–8452, https://doi.org/10.5194/acp-23-8429-2023, 2023.

European Commission, Joint Research Centre (JRC), the International Energy Agency (IEA): EDGAR (Emissions Database for Global Atmospheric Research) Community GHG Database, comprising IEA-EDGAR CO2, EDGAR CH4, EDGAR N2O, EDGAR F-GASES version 8.0,, https://edgar.jrc.ec.europa.eu/report_2023, 2023.

France, J. L., Cain, M., Fisher, R. E., Lowry, D., Allen, G., O'Shea, S. J., Illingworth, S., Pyle, J., Warwick, N., Jones, B. T., Gallagher, M. W., Bower, K., Le Breton, M., Percival, C., Muller, J., Welpott, A., Bauguitte, S., George, C., Hayman, G. D., Manning, A. J., Myhre, C. L., Lanoisellé, M., and Nisbet, E. G.: Measurements of δ^{13}C in CH_4 and using particle dispersion modeling to characterize sources of Arctic methane within an air mass, J. Geophys. Res.-Atmos., 121, https://doi.org/10.1002/2016JD026006, 2016.

Ganesan, A. L., Rigby, M., Zammit-Mangion, A., Manning, A. J., Prinn, R. G., Fraser, P. J., Harth, C. M., Kim, K.-R., Krummel, P. B., Li, S., Mühle, J., O'Doherty, S. J., Park, S., Salameh, P. K., Steele, L. P., and Weiss, R. F.: Characterization of uncertainties in atmospheric trace gas inversions using hierarchical Bayesian methods, Atmos. Chem. Phys., 14, 3855–3864, https://doi.org/10.5194/acp-14-3855-2014, 2014.

Ganesan, A. L., Manning, A. J., Grant, A., Young, D., Oram, D. E., Sturges, W. T., Moncrieff, J. B., and O'Doherty, S.: Quantifying methane and nitrous oxide emissions from the UK and Ireland using a national-scale monitoring network, Atmos. Chem. Phys., 15, 6393–6406, https://doi.org/10.5194/acp-15-6393-2015, 2015.

Ganesan, A. L., Schwietzke, S., Poulter, B., Arnold, T., Lan, X., Rigby, M., Vogel, F. R., Werf, G. R., Janssens-Maenhout, G., Boesch, H., Pandey, S., Manning, A. J., Jackson, R. B., Nisbet, E. G., and Manning, M. R.: Advancing Scientific Understanding of the Global Methane Budget in Support of the Paris Agreement, Glob. Biogeochem. Cycles., 33, 1475–1512, https://doi.org/10.1029/2018GB006065, 2019.

Henne, S., Brunner, D., Oney, B., Leuenberger, M., Eugster, W., Bamberger, I., Meinhardt, F., Steinbacher, M., and Emmenegger, L.: Validation of the Swiss methane emission inventory by atmospheric observations and inverse modelling, Atmos. Chem. Phys., 16, 3683–3710, https://doi.org/10.5194/acp-16-3683-2016, 2016.

Hoheisel, A. and Schmidt, M.: Six years of continuous carbon isotope composition measurements of methane in Heidelberg (Germany) – a study of source contributions and comparison to emission inventories, Atmos. Chem. Phys., 24, 2951–2969, https://doi.org/10.5194/acp-24-2951-2024, 2024.

ICOS RI, Apadula, F., Arnold, S., Arriga, N., Bergamaschi, P., Biermann, T., Blandin, E., Blessing, C., Bracci, A., Busetto, M., Bán, S., Bäni, L., Calzolari, F., Chen, H., Colomb, A., Conen, F., Conil, S., Couret, C., Cristofanelli, P., De Mazière, M., Delmotte, M., Di Iorio, T., Elsasser, M., Emmenegger, L., Forster, G., Fratticioli, C., Friedli, J., Frumau, A., Fuente-Lastra, M., Gest, L., Grossmann, J., Hanuš, V., Harris, E., Haszpra, L., Hatakka, J., Heliasz, M., Helle, J., Heltai, D., Hensen, A., Hermans, C., Hermansen, O., Hoheisel, A., Kazan, V., Keronen, P., Kneuer, T., Kolari, P., Komínková, K., Kubistin, D., Kumps, N., Laitinen, A., Langrene, L., Lanza, A., Larmanou, E., Laurent, O., Laurila, T., Legendre, V., Lehner, I., Lehtinen, K., Leskinen, A., Leuenberger, M., Levula, J., Lindauer, M., Lopez, D.,

Lopez, M., Lund Myhre, C., Lunder, C., Mammarella, I., Manca, G., Mandrick, Z., Manning, A., Marek, M., Marklund, P., Meinhardt, F., Metzger, J.-M., Miettinen, P., Molder, M., Molnár, M., Montaguti, S., Mölder, M., Müller-Williams, J., O'Doherty, S., Ottosson-Löfvenius, M., Piacentino, S., Pichon, J.-M., Pitt, J., Platt, S., Plaß-Dülmer, C., Ramonet, M., Rigouleau, L.-J., Rivas-Soriano, P., Roulet, Y.-A., Scheeren, B., Schmidt, M., Schreiber, M., Schumacher, M., Sferlazzo, D., Sha, M., Smith, P., Stanley, K., Steger, D., Steinbacher, M., Sørensen, L., Taipale, R., Trisolino, P., Vermeulen, A., Vítková, G., Weyrauch, D., Ylisirniö, A., Yver-Kwok, C., Zazzeri, G., Zwerschke, E., di Sarra, A., van den Bulk, P., and Álvarez Hernández, A.: European Obspack compilation of atmospheric carbon dioxide, methane, nitrous oxide and carbon monoxide data from ICOS stations for the period 1972-2025; obspack_466_ICOSFT2025.3_20251003, https://doi.org/10.18160/46ST-DEVK, 2025.

Jones, A., Thomson, D., Hort, M., and Devenish, B.: The U.K. Met Office's Next-Generation Atmospheric Dispersion Model, NAME III, in: Air Pollution Modeling and Its Application XVII, edited by Borrego, C. and Norman, A.-L., pp. 580–589, Springer US, Boston, MA, ISBN 978-0-387-68854-1, 2007.

Lan, X., Basu, S., Schwietzke, S., Bruhwiler, L. M. P., Dlugokencky, E. J., Michel, S. E., Sherwood, O. A., Tans, P. P., Thoning, K., Etiope, G., Zhuang, Q., Liu, L., Oh, Y., Miller, J. B., Pétron, G., Vaughn, B. H., and Crippa, M.: Improved Constraints on Global Methane Emissions and Sinks Using δ^{14}C-CH_4, Glob. Biogeochem. Cycles., 35, https://doi.org/10.1029/2021GB007000, 2021.

Lan, X., Thoning, K., and Dlugokencky, E.: Trends in globally-averaged CH4, N2O, and SF6 determined from NOAA Global Monitoring Laboratory measurements. Version 2023-01, https://doi.org/10.15138/P8XG-AA10, 2023.

Leip, A., Skiba, U., Vermeulen, A., and Thompson, R. L.: A complete rethink is needed on how greenhouse gas emissions are quantified for national reporting, Atmospheric Environment, 174, 237–240, https://doi.org/10.1016/j.atmosenv.2017.12.006, 2018.

Levy, P.: UKGHG, https://github.com/NERC-CEH/ukghg, 2020.

Lowry, D., Fisher, R. E., France, J. L., Coleman, M., Lanoisellé, M., Zazzeri, G., Nisbet, E. G., Shaw, J. T., Allen, G., Pitt, J., and Ward, R. S.: Environmental baseline monitoring for shale gas development in the UK: Identification and geochemical characterisation of local source emissions of methane to atmosphere, Sci. Total Environ., 708, 134 600, https://doi.org/10.1016/j.scitotenv.2019.134600, 2020.

Lunt, M. F., Manning, A. J., Allen, G., Arnold, T., Bauguitte, S. J.-B., Boesch, H., Ganesan, A. L., Grant, A., Helfter, C., Nemitz, E., O'Doherty, S. J., Palmer, P. I., Pitt, J. R., Rennick, C., Say, D., Stanley, K. M., Stavert, A. R., Young, D., and Rigby, M.: Atmospheric observations consistent with reported decline in the UK's methane emissions (2013–2020), Atmos. Chem. Phys., 21, 16 257–16 276, https://doi.org/10.5194/acp-21-16257-2021, 2021.

Maasakkers, J. D., Jacob, D. J., Sulprizio, M. P., Scarpelli, T. R., Nesser, H., Sheng, J.-X., Zhang, Y., Hersher, M., Bloom, A. A., Bowman, K. W., Worden, J. R., Janssens-Maenhout, G., and Parker, R. J.: Global distribution of methane emissions, emission trends, and OH concentrations and trends inferred from an inversion of GOSAT satellite data for 2010–2015, Atmos. Chem. Phys., 19, 7859–7881, https://doi.org/10.5194/acp-19-7859-2019, 2019.

Manning, A. J., Redington, A. L., Say, D., O'Doherty, S., Young, D., Simmonds, P. G., Vollmer, M. K., Mühle, J., Arduini, J., Spain, G., Wisher, A., Maione, M., Schuck, T. J., Stanley, K., Reimann, S., Engel, A., Krummel, P. B., Fraser, P. J., Harth, C. M., Salameh, P. K., Weiss, R. F., Gluckman, R., Brown, P. N., Watterson, J. D., and Arnold, T.: Evidence of a recent decline in UK emissions of hydrofluorocarbons determined by the InTEM inverse model and atmospheric measurements, Atmos. Chem. Phys., 21, 12 739–12 755, https://doi.org/10.5194/acp-21-12739-2021, 2021.

Menoud, M., van der Veen, C., Necki, J., Bartyzel, J., Szénási, B., Stanisavljević, M., Pison, I., Bousquet, P., and Röckmann, T.: Methane (CH_4) sources in Krakow, Poland: insights from isotope analysis, Atmos. Chem. Phys., 21, 13 167–13 185, https://doi.org/10.5194/acp-21-13167-2021, 2021.

Menoud, M., van der Veen, C., Lowry, D., Fernandez, J. M., Bakkaloglu, S., France, J. L., Fisher, R. E., Maazallahi, H., Stanisavljević, M., Nęcki, J., Vinkovic, K., Łakomiec, P., Rinne, J., Korbeń, P., Schmidt, M., Defratyka, S., Yver-Kwok, C., Andersen, T., Chen, H., and Röckmann, T.: New contributions of measurements in Europe to the global inventory of the stable isotopic composition of methane, Earth Syst. Sci. Data, 14, 4365–4386, https://doi.org/10.5194/essd-14-4365-2022, 2022.

Michel, S., Clark, J., Vaughn, B., Crotwell, M., Madronich, M., Moglia, E., Neff, D., and Mund, J.: University of Colorado, Institute of Arctic and Alpine Research (INSTAAR). Stable Isotopic Composition of Atmospheric Methane (13C) from the NOAA GML Carbon Cycle Cooperative Global Air Sampling Network, 1998-2022 Version: 2023-09-21, https://doi.org/10.15138/9p89-1x02, 2023.

Mielke-Maday, I., Schwietzke, S., Yacovitch, T., Miller, B., Conley, S., Kofler, J., Handley, P., Thorley, E., Herndon, S. C., Hall, B., Dlugokencky, E., Lang, P., Wolter, S., Moglia, E., Crotwell, M., Crotwell, A., Rhodes, M., Kitzis, D., Vaughn, T., Bell, C., Zimmerle, D., Schnell, R., and Pétron, G.: Methane source attribution in a U.S. dry gas basin using spatial patterns of ground and airborne ethane and methane measurements, Elem Sci Anth, 7, 13, https://doi.org/10.1525/elementa.351, 2019.

Milkov, A. V., Schwietzke, S., Allen, G., Sherwood, O. A., and Etiope, G.: Using global isotopic data to constrain the role of shale gas production in recent increases in atmospheric methane, Sci Rep, 10, 1–7, https://doi.org/10.1038/s41598-020-61035-w, 2020.

Myhre, G., Shindell, D., Bréon, F.-M., Collins, W., Fuglestvedt, J., J. Huang, D. K., Lamarque, J.-F., Lee, D., Mendoza, B., Nakajima, T., Robock, A., Stephens, G., Takemura, T., and Zhang, H.: 2013: Anthropogenic and Natural Radiative Forcing. In: Climate Change 2013: The Physical Science Basis. Contribution of Working Group I to the Fifth Assessment Report of the Intergovernmental Panel on Climate Change, Tech. rep., Intergovernmental Panel on Climate Change, Cambridge, United Kingdom and New York, NY, USA, 2013.

Nisbet, E. G., Manning, M. R., Dlugokencky, E. J., Fisher, R. E., Lowry, D., Michel, S. E., Myhre, C. L., Platt, S. M., Allen, G., Bousquet, P., Brownlow, R., Cain, M., France, J. L., Hermansen, O., Hossaini, R., Jones, A. E., Levin, I., Manning, A. C., Myhre, G., Pyle, J. A., Vaughn, B. H., Warwick, N. J., and White, J. W. C.: Very Strong Atmospheric Methane Growth in the 4 Years 2014–2017: Implications for the Paris Agreement, Glob. Biogeochem. Cycles., 33, 318–342, https://doi.org/10.1029/2018GB006009, 2019.

PARIS: Process Attribution of Regional Emissions (PARIS), https://horizoneurope-paris.eu/, 2023.

Pison, I., Ringeval, B., Bousquet, P., Prigent, C., and Papa, F.: Stable atmospheric methane in the 2000s: key-role of emissions from natural wetlands, Atmos. Chem. Phys., 13, 11 609–11 623, https://doi.org/10.5194/acp-13-11609-2013, 2013.

Ramsden, A. E.: multiple_gas_inverse_model v1.0 (Version v1), https://doi.org/10.5281/zenodo.18496508, 2026.

Ramsden, A. E., Ganesan, A. L., Western, L. M., Rigby, M., Manning, A. J., Foulds, A., France, J. L., Barker, P., Levy, P., Say, D., Wisher, A., Arnold, T., Rennick, C., Stanley, K. M., Young, D., and O'Doherty, S.: Quantifying fossil fuel methane emissions using observations of atmospheric ethane and an uncertain emission ratio, Atmos. Chem. Phys., 22, 3911–3929, https://doi.org/10.5194/acp-22-3911-2022, 2022.

Rennick, C., Arnold, T., Safi, E., Drinkwater, A., Dylag, C., Webber, E. M., Hill-Pearce, R., Worton, D. R., Bausi, F., and Lowry, D.: Boreas: A Sample Preparation-Coupled Laser Spectrometer System for Simultaneous High-Precision In Situ Analysis of δ^{13}C and δ^{2}H from Ambient Air Methane, Anal. Chem., 93, 10 141–10 151, https://doi.org/10.1021/acs.analchem.1c01103, 2021.

Rennick, C., Arnold, T., Chung, E., Safi, E., and Kikaj, D.: Atmospheric GHG data product (ch4, ch4_stdev, 13ch4, 13ch4_stdev, d2h_ch4, d2h_ch4_stdev) from Heathfield (100.0 m), https://doi.org/11676/MRHwmQFqm0O_Y39065JsIQLS, 2025.

Riddell-Young, B., Lan, X., Sherwood, O. A., and Laboratory, N. G. M.: Global Inventory of Fossil and Non-fossil Methane δ13C and δD Source Signature Measurements for Improved Atmospheric Modeling, version 2025 [Data set], https://doi.org/10.15138/92GG-EY58, 2025a.

Riddell-Young, B., Michel, S. E., Lan, X., Tans, P., Röckmann, T., Dasgupta, B., Oh, Y., Bruhwiler, L. M. P., Fujita, R., Umezawa, T., Morimoto, S., and Miller, J. B.: Microbial driver of 2006–2023 CH_4 growth indicated by trends in atmospheric δD–CH_4 and δ^{13}C–CH_4, Proc. Natl. Acad. Sci. U.S.A., 122, https://doi.org/10.1073/pnas.2516543122, 2025b.

Röckmann, T., Eyer, S., van der Veen, C., Popa, M. E., Tuzson, B., Monteil, G., Houweling, S., Harris, E., Brunner, D., Fischer, H., Zazzeri, G., Lowry, D., Nisbet, E. G., Brand, W. A., Necki, J. M., Emmenegger, L., and Mohn, J.: In situ observations of the isotopic composition of methane at the Cabauw tall tower site, Atmos. Chem. Phys., 16, 10 469–10 487, https://doi.org/10.5194/acp-16-10469-2016, 2016.

Saboya, E., Zazzeri, G., Graven, H., Manning, A. J., and Michel, S. E.: Continuous CH_4 and δ^{13}C Measurements in London Demonstrate Under-Reported Natural Gas Leakage, Atmos. Chem. Phys., 22, 3595–3613, https://doi.org/10.5194/acp-22-3595-2022, 2021.

Safi, E., Arnold, T., and Rennick, C.: Fractionation of Methane Isotopologues during Preparation for Analysis from Ambient Air, Anal. Chem., https://doi.org/10.1021/acs.analchem.3c04891, publisher: American Chemical Society, 2024.

Saunois, M., Martinez, A., Poulter, B., Zhang, Z., Raymond, P., Regnier, P., Canadell, J. G., Jackson, R. B., Patra, P. K., Bousquet, P., Ciais, P., Dlugokencky, E. J., Lan, X., Allen, G. H., Bastviken, D., Beerling, D. J., Belikov, D. A., Blake, D. R., Castaldi, S., Crippa, M., Deemer, B. R., Dennison, F., Etiope, G., Gedney, N., Höglund-Isaksson, L., Holgerson, M. A., Hopcroft, P. O., Hugelius, G., Ito, A., Jain, A. K., Janardanan, R., Johnson, M. S., Kleinen, T., Krummel, P., Lauerwald, R., Li, T., Liu, X., McDonald, K. C., Melton, J. R., Mühle, J., Müller, J., Murguia-Flores, F., Niwa, Y., Noce, S., Pan, S., Parker, R. J., Peng, C., Ramonet, M., Riley, W. J., Rocher-Ros, G., Rosentreter, J. A., Sasakawa, M., Segers, A., Smith, S. J., Stanley, E. H., Thanwerdas, J., Tian, H., Tsuruta, A., Tubiello, F. N., Weber, T. S., Van Der Werf, G., Worthy, D. E., Xi, Y., Yoshida, Y., Zhang, W., Zheng, B., Zhu, Q., Zhu, Q., and Zhuang, Q.: Global Methane Budget 2000–2020, Earth Syst. Sci. Data, 17, 1873–1958, https://doi.org/10.5194/essd-17-1873-2025, 2025.

Schaefer, H., Fletcher, S. E. M., Veidt, C., Lassey, K. R., Brailsford, G. W., Bromley, T. M., Dlugokencky, E. J., Michel, S. E., Miller, J. B., Levin, I., Lowe, D. C., Martin, R. J., Vaughn, B. H., and White, J. W. C.: A 21st-century shift from fossil-fuel to biogenic methane emissions indicated by 13CH4, Science, 352, 80–84, https://doi.org/10.1126/science.aad2705, 2016.

Sheng, J.-X., Jacob, D. J., Turner, A. J., Maasakkers, J. D., Sulprizio, M. P., Bloom, A. A., Andrews, A. E., and Wunch, D.: High-resolution inversion of methane emissions in the Southeast US using SEAC^{4}RS aircraft observations of atmospheric methane: anthropogenic and wetland sources, Atmos. Chem. Phys., 18, 6483–6491, https://doi.org/10.5194/acp-18-6483-2018, 2018.

Sherwood, O. A., Schwietzke, S., Arling, V. A., and Etiope, G.: Global Inventory of Gas Geochemistry Data from Fossil Fuel, Microbial and Burning Sources, version 2017, Earth Syst. Sci. Data, 9, 639–656, https://doi.org/10.5194/essd-9-639-2017, 2017.

Stanley, K. M., Grant, A., O'Doherty, S., Young, D., Manning, A. J., Stavert, A. R., Spain, T. G., Salameh, P. K., Harth, C. M., Simmonds, P. G., Sturges, W. T., Oram, D. E., and Derwent, R. G.: Greenhouse gas measurements from a UK network of tall towers: technical description and first results, Atmos. Meas. Tech., 11, 1437–1458, https://doi.org/10.5194/amt-11-1437-2018, 2018.

Stavert, A. R., O'Doherty, S., Stanley, K., Young, D., Manning, A. J., Lunt, M. F., Rennick, C., and Arnold, T.: UK greenhouse gas measurements at two new tall towers for aiding emissions verification, Atmos. Meas. Tech., 12, 4495–4518, https://doi.org/10.5194/amt-12-4495-2019, 2019.

Thanwerdas, J., Saunois, M., Berchet, A., Pison, I., Vaughn, B. H., Michel, S. E., and Bousquet, P.: Variational inverse modeling within the Community Inversion Framework v1.1 to assimilate δ^{13}C(CH_4) and CH_4: a case study with model LMDz-SACS, Geosci. Model Dev., 15, 4831–4851, https://doi.org/10.5194/gmd-15-4831-2022, 2022.

Thanwerdas, J., Saunois, M., Berchet, A., Pison, I., and Bousquet, P.: Investigation of the renewed methane growth post-2007 with high-resolution 3-D variational inverse modeling and isotopic constraints, Atmos. Chem. Phys., 24, 2129–2167, https://doi.org/10.5194/acp-24-2129-2024, 2024.

Tunnicliffe, R. L., Ganesan, A. L., Parker, R. J., Boesch, H., Gedney, N., Poulter, B., Zhang, Z., Lavrič, J. V., Walter, D., Rigby, M., Henne, S., Young, D., and O'Doherty, S.: Quantifying sources of Brazil's CH_4 emissions between 2010 and 2018 from satellite data, Atmos. Chem. Phys., 20, 13 041–13 067, https://doi.org/10.5194/acp-20-13041-2020, 2020.

Varga, T., Fisher, R. E., France, J. L., Haszpra, L., Jull, A. J. T., Lowry, D., Major, I., Molnár, M., Nisbet, E. G., and László, E.: Identification of Potential Methane Source Regions in Europe Using $\delta^{13}C_{CH4}$ Measurements and Trajectory Modeling, J. Geophys. Res.-Atmos., 126, https://doi.org/10.1029/2020JD033963, 2021.

Walters, D. N., Williams, K. D., Boutle, I. A., Bushell, A. C., Edwards, J. M., Field, P. R., Lock, A. P., Morcrette, C. J., Stratton, R. A., Wilkinson, J. M., Willett, M. R., Bellouin, N., Bodas-Salcedo, A., Brooks, M. E., Copsey, D., Earnshaw, P. D., Hardiman, S. C., Harris, C. M., Levine, R. C., MacLachlan, C., Manners, J. C., Martin, G. M., Milton, S. F., Palmer, M. D., Roberts, M. J., RodrÃguez, J. M., Tennant, W. J., and Vidale, P. L.: The Met Office Unified Model Global Atmosphere 4.0 and JULES Global Land 4.0 configurations, Geosci. Model Dev., 7, 361–386, https://doi.org/10.5194/gmd-7-361-2014, 2014.

Werner, R. A. and Brand, W. A.: Referencing Strategies and Techniques in Stable Isotope Ratio Analysis, Rapid Commun. Mass Spectrom., 17, 501–519, https://doi.org/10.1002/rcm.258, 2001.

Western, L. M., Ramsden, A. E., Ganesan, A. L., Boesch, H., Parker, R. J., Scarpelli, T. R., Tunnicliffe, R. L., and Rigby, M.: Estimates of North African Methane Emissions from 2010 to 2017 Using GOSAT Observations, Environ. Sci. Technol. Lett., https://doi.org/10.1021/acs.estlett.1c00327, publisher: American Chemical Society, 2021.

Zazzeri, G., Lowry, D., Fisher, R. E., France, J. L., Lanoisellé, M., Grimmond, C. S. B., and Nisbet, E. G.: Evaluating methane inventories by isotopic analysis in the London region, Sci Rep, 7, 4854, https://doi.org/10.1038/s41598-017-04802-6, 2017.

Zhang, Y., Jacob, D. J., Lu, X., Maasakkers, J. D., Scarpelli, T. R., Sheng, J.-X., Shen, L., Qu, Z., Sulprizio, M. P., Chang, J., Bloom, A. A., Ma, S., Worden, J., Parker, R. J., and Boesch, H.: Attribution of the accelerating increase in atmospheric methane during 2010–2018 by inverse analysis of GOSAT observations, Atmos. Chem. Phys., 21, 3643–3666, https://doi.org/10.5194/acp-21-3643-2021, 2021.